

Preparation of $\text{Ba}_{0.5}\text{Sr}_{0.5}(\text{Co}_{0.8}\text{Fe}_{0.2})_{1-x}\text{Ta}_x\text{O}_{3-\delta}$ perovskite anode for solid oxide electrolysis cell and comparison of electrochemical performance and durability with the basic anodes



A Thesis Submitted in Partial Fulfillment of the Requirements
for the Degree of Master of Engineering in Chemical Engineering

Department of Chemical Engineering

FACULTY OF ENGINEERING

Chulalongkorn University

Academic Year 2019

Copyright of Chulalongkorn University

การเตรียมขั้วแอโนดชนิดเพอรอฟสไกต์ $Ba_{0.5}Sr_{0.5}(Co_{0.8}Fe_{0.2})_{1-x}Ta_xO_{3-\delta}$ สำหรับเซลล์อิเล็กโทรไลซิส
แบบออกไซด์ของแข็งและการเปรียบเทียบความสามารถทางเคมีไฟฟ้าและความคงทนกับขั้วแอโนด
พื้นฐาน



วิทยานิพนธ์นี้เป็นส่วนหนึ่งของการศึกษาตามหลักสูตรปริญญาวิศวกรรมศาสตรมหาบัณฑิต
สาขาวิชาวิศวกรรมเคมี ภาควิชาวิศวกรรมเคมี
คณะวิศวกรรมศาสตร์ จุฬาลงกรณ์มหาวิทยาลัย
ปีการศึกษา 2562
ลิขสิทธิ์ของจุฬาลงกรณ์มหาวิทยาลัย

Thesis Title Preparation of $Ba_{0.5}Sr_{0.5}(Co_{0.8}Fe_{0.2})_{1-x}Ta_xO_{3-\delta}$ perovskite anode for solid oxide electrolysis cell and comparison of electrochemical performance and durability with the basic anodes

By Miss Patthiya Prasopchokkul

Field of Study Chemical Engineering

Thesis Advisor Assistant Professor PATTARAPORN KIM, Ph.D.

Accepted by the FACULTY OF ENGINEERING, Chulalongkorn University in Partial Fulfillment of the Requirement for the Master of Engineering

..... Dean of the FACULTY OF ENGINEERING
(Professor SUPOT TEACHAVORASINSKUN, D.Eng.)

THESIS COMMITTEE

..... Chairman
(Assistant Professor SUPHOT PHATANASRI, Ph.D.)

..... Thesis Advisor
(Assistant Professor PATTARAPORN KIM, Ph.D.)

..... Examiner
(Professor BUNJERD JONGSOMJIT, Ph.D.)

..... External Examiner
(Assistant Professor Panpailin Seeharaj, Ph.D.)

จุฬาลงกรณ์มหาวิทยาลัย
CHULALONGKORN UNIVERSITY

ภัททิยา ประสพโชคกุล : การเตรียมขั้วแอโนดชนิดเพอโรฟสไกต์ $Ba_{0.5}Sr_{0.5}(Co_{0.8}Fe_{0.2})_{1-x}Ta_xO_{3-\delta}$ สำหรับเซลล์อิเล็กโทรไลซิสแบบออกไซด์ของแข็งและการเปรียบเทียบความสามารถทางเคมีไฟฟ้าและความทนทานกับขั้วแอโนดพื้นฐาน . (Preparation of $Ba_{0.5}Sr_{0.5}(Co_{0.8}Fe_{0.2})_{1-x}Ta_xO_{3-\delta}$ perovskite anode for solid oxide electrolysis cell and comparison of electrochemical performance and durability with the basic anodes) อ.ที่ปรึกษาหลัก : ภัทรพร คิม

ขั้วแอโนดชนิดเพอโรฟสไกต์ $Ba_{0.5}Sr_{0.5}Co_{0.8}Fe_{0.2}O_{3-\delta}$ (BSCF) จัดเป็นขั้วแอโนดชนิดหนึ่งที่ได้รับ ความสนใจเป็นอย่างยิ่งเนื่องจากมีประสิทธิภาพสำหรับใช้ในเซลล์อิเล็กโทรไลซิสแบบออกไซด์ของแข็งค่อนข้างสูง แต่อย่างไรก็ตามขั้วแอโนดชนิด BSCF ยังคงขาดเสถียรภาพทางโครงสร้างเคมีซึ่งส่งผลถึงความทนทานในการใช้งาน ดังนั้นเพื่อทำการพัฒนาและปรับปรุงข้อบกพร่องนี้ จึงทำการสังเคราะห์ $Ba_{0.5}Sr_{0.5}(Co_{0.8}Fe_{0.2})_{1-x}Ta_xO_{3-\delta}$ โดยการเติมไอออนโลหะ Ta ที่ตำแหน่ง B (Co และ Fe) เมื่อ x มีค่าเท่ากับ 5 10 15 และ 20 เปอร์เซ็นต์โมล ด้วยวิธีซีเทรตอิตาลีทีเอ จากการวิเคราะห์ด้วยเทคนิคสเปกตรัมของรังสีเอ็กซ์พบว่าตัวอย่างชนิด BSCF และ BSCFTa0.05 แสดงโครงสร้างเพอโรฟสไกต์แบบผลึกเดียว ในขณะที่เดียวกันได้เกิดสารประกอบ Ta_2O_5 และ Ta_3N_5 ขึ้นในตัวอย่างอื่นๆ การขึ้นรูปเซลล์แบบครึ่งเซลล์สมมาตร โดยประกอบด้วยชั้นอิเล็กโทรไลต์ชนิด YSZ และขั้วอิเล็กโทรด BSCFTa (BSCFTa/YSZ/BSCFTa) เพื่อหาความต้านทานต่อพื้นที่ของขั้วอิเล็กโทรด จากการทดสอบที่อุณหภูมิ 600 องศาเซลเซียสพบว่าขั้วแอโนดชนิด BSCFTa0.10 มีค่าความต้านทานต่อพื้นที่น้อยที่สุด โดยมีค่าเท่ากับ 2.32 โอห์มต่อตารางเซนติเมตร และเมื่อเปรียบเทียบความสามารถทางเคมีไฟฟ้าและความทนทานของเซลล์อิเล็กโทรไลซิสแบบออกไซด์ของแข็งซึ่งประกอบด้วยขั้วแคโทดชนิด Ni-YSZ ชั้นอิเล็กโทรไลต์ชนิด YSZ และขั้วแอโนดทั้ง 3 ชนิด ได้แก่ BSCF และ LSM-YSZ ซึ่งเป็นขั้วแอโนดชนิดพื้นฐานกับขั้วแอโนดชนิด BSCFTa0.10 พบว่าเซลล์อิเล็กโทรไลซิสแบบออกไซด์ของแข็งที่ประกอบด้วยขั้วแอโนดชนิด BSCFTa0.10 (Ni-YSZ/YSZ/BSCFTa0.10) มีความสามารถทางเคมีไฟฟ้าและความทนทานที่ดีที่สุด โดยที่อุณหภูมิในการทำงานที่ 800 องศาเซลเซียส ภายใต้อัตราส่วนของไอน้ำต่อไฮโดรเจนที่ 70:30 และป้อนความหนาแน่นกระแสไฟฟ้าที่ 0.45 แอมป์ต่อตารางเซนติเมตรเป็นเวลา 80 ชั่วโมง พบว่าอัตราการเสื่อมของเซลล์อิเล็กโทรไลซิสชนิด Ni-YSZ/YSZ/BSCF Ni-YSZ/YSZ/BSCFTa0.10 และ Ni-YSZ/YSZ/LSM-YSZ มีค่าเท่ากับ 0.0123 0.0027 และ 0.0204 โวลต์ต่อชั่วโมงตามลำดับ ดังนั้นการเติมไอออนโลหะที่มีค่าวาเลนซ์สูงอย่าง Ta จะช่วยเพิ่มความทนทานและเสถียรภาพทางโครงสร้างเคมีของเพอโรฟสไกต์ชนิด BSCF เนื่องจากการเติมไอออนโลหะ Ta ส่งผลทำให้ที่ว่างของออกซิเจนในโครงสร้างเพอโรฟสไกต์นั้นลดลง แต่อย่างไรก็ตามความสามารถทางเคมีไฟฟ้าก็เพิ่มขึ้นด้วยเมื่อเติมไอออนโลหะ Ta ลงใน BSCF ซึ่งเป็นผลมาจากการรักษาสมดุลที่เหมาะสมระหว่างการนำไฟฟ้าและการนำไอออนในขั้วแอโนดชนิด BSCFTa0.10

สาขาวิชา วิศวกรรมเคมี

ลายมือชื่อนิสิต

ปีการศึกษา 2562

ลายมือชื่อ อ.ที่ปรึกษาหลัก

6170390021 : MAJOR CHEMICAL ENGINEERING

KEYWORD: Solid oxide electrolysis cell, Phase stability, perovskites, Tantalum doped barium strontium cobalt ferrite, BSCFTa

Patthiya Prasopchokkul : Preparation of $\text{Ba}_{0.5}\text{Sr}_{0.5}(\text{Co}_{0.8}\text{Fe}_{0.2})_{1-x}\text{Ta}_x\text{O}_{3-\delta}$ perovskite anode for solid oxide electrolysis cell and comparison of electrochemical performance and durability with the basic anodes. Advisor: Asst. Prof. PATTARAPORN KIM, Ph.D.

Among perovskite anodes in solid oxide electrolysis cell (SOEC), $\text{Ba}_{0.5}\text{Sr}_{0.5}\text{Co}_{0.8}\text{Fe}_{0.2}\text{O}_{3-\delta}$ (BSCF) has gained much attention due to its relatively high performance. However, the BSCF still suffers from chemical instability. In this study, partial substituting higher valance Ta^{5+} (5, 10, 15 and 20 mol%) at the B-site ($\text{Co}^{2+}/\text{Fe}^{3+}$) of BSCF was investigated to improve its structural stability. The $\text{Ba}_{0.5}\text{Sr}_{0.5}(\text{Co}_{0.8}\text{Fe}_{0.2})_{1-x}\text{Ta}_x\text{O}_{3-\delta}$ (BSCFTax, $0 \leq x \leq 0.20$) were synthesized by citrate-EDTA complexing method. The BSCF and BSCFTa0.05 exhibited the single phase perovskite while segregation of Ta_2O_5 and Ta_3N_5 were observed in other samples. The symmetrical half-cell having the yttria stabilized zirconia (YSZ) as an electrolyte (BSCFTa/YSZ/BSCFTa) were fabricated to determine the area specific resistance (ASR) of the electrode. BSCFTa0.10 shows the lowest ASR of $2.32 \Omega\cdot\text{cm}^2$ at 600°C . Comparing electrochemical performance and durability of single cells having undoped BSCF, BSCFTa0.10 and LSM-YSZ a basic anode, Ni-YSZ/YSZ/BSCFTa0.10 exhibited the highest performance and durability. The degradation rate of Ni-YSZ/YSZ/BSCF, Ni-YSZ/YSZ/BSCFTa0.10 and Ni-YSZ/YSZ/LSM-YSZ were $0.0123\text{V}\cdot\text{h}^{-1}$, $0.0027\text{V}\cdot\text{h}^{-1}$ and $0.0204\text{V}\cdot\text{h}^{-1}$, respectively (operating at current density $0.45\text{A}\cdot\text{cm}^{-2}$ in electrolysis mode, 80 h, 800°C and H_2O to H_2 ratio of 70:30). Doping with higher valance Ta^{5+} increased durability and chemical stability in BSCF but also decreased oxygen vacancy due to decreasing defect in the perovskite. However, electrochemical performance increased in Ta^{5+} doped BSCF, likely due to a proper balance between electronic and ionic conductivity in doped BSCF.

Field of Study: Chemical Engineering

Student's Signature

Academic Year: 2019

Advisor's Signature

ACKNOWLEDGEMENTS

I would like to express my sincere gratitude to my advisor, Asst. Prof. Dr. Pattaraporn Kimlohsontorn for her valuable advice, useful guidance, kind suggestions, and her intensive care throughout this research. I gratefully thank to PTT hydrogen SOEC project group for the opportunity that gave a moment for valuable brainstorm discussion and recommendation in any problem on my experiment. In addition, I also gratefully acknowledge to PTT public company limited for supporting a research fund.

I would like to thank to scientists, staff in Center of Excellence on Catalysis and Catalytic Reaction Engineering (CECC), Department of chemical engineering, Chulalongkorn University for supporting many instruments.

Finally, I would like to special thanks to my family and my lovely friends for encouraging me with their best wishes and always there cheering me up. Moreover, I would like to appreciate myself for being patient and my hard effort throughout the course of my research and study. This chapter of life is very challenging and makes my life interesting. Overcoming them is make me known that myself enough to respect and meaningful.

Patthiya Prasopchokkul

TABLE OF CONTENTS

	Page
ABSTRACT (THAI).....	iii
ABSTRACT (ENGLISH).....	iv
ACKNOWLEDGEMENTS.....	v
TABLE OF CONTENTS.....	vi
LIST OF FIGURES.....	x
LIST OF TABLES.....	xiii
CHAPTER I.....	1
1.1 Motivation.....	1
1.2 Research objectives.....	3
1.3 Research scopes.....	3
1.4 Expected benefit.....	3
CHAPTER II.....	5
2.1 SOEC.....	5
2.1.1 Principle of operation.....	5
2.1.2 SOEC component requirements.....	6
2.1.2.1 Electrolyte materials.....	6
2.1.2.2 Cathode materials.....	6
2.1.2.3 Anode materials.....	6
2.2 Structure of perovskites.....	8
2.2.1 Crystal structure.....	8
2.2.2 Tolerance factors in perovskites.....	9

2.2.3 Non-stoichiometry in perovskites	10
2.3 Metal doping at A and B site of BSCF	10
2.3.1 W-doped BSCF	11
2.3.2 Mo-doped BSCF	12
2.3.3 Ti-doped BSCF	14
2.3.4 Nb-doped BSCF	14
2.3.5 Ta-doped BSCF	16
2.4 Perovskite synthesis	17
2.4.1 Solid state reaction	17
2.4.2 Wet chemical synthesis	18
2.4.2.1 Solution combustion	18
2.4.2.2 Co-precipitation	18
2.4.2.3 Citrate-EDTA complexing method.....	19
CHAPTER III	20
3.1 Chemicals.....	20
3.2 Cathode preparation	22
3.3 Electrolyte preparation	23
3.4 Synthesis of perovskite anode powder by citrate-EDTA complexing method...	23
3.5 Solid oxide electrolysis cell fabrication.....	25
3.5.1 Symmetrical half-cells fabrication.....	25
3.5.2 Single cell fabrication.....	25
3.6 Characterization of anode perovskite	26
3.6.1 X-ray diffraction (XRD).....	26
3.6.2 X-ray photoelectron spectroscopy (XPS).....	26

3.6.3 Brunauer-Emmett-Teller (BET)	26
3.6.4 Scanning electron microscope (SEM).....	26
3.6.5 Thermogravimetric analysis (TGA)	27
3.6.6 Electrochemical performance measurements.....	27
CHAPTER IV	29
4.1 Structural characterization	29
4.2 Thermogravimetric analysis.....	32
4.3 X-ray photoelectron spectroscopy analysis	34
4.4 Calculation of tolerance factor (t).....	37
4.5 Electrochemical performance	38
4.5.1 Electrochemical performance of symmetrical half-cell.....	38
4.5.2 Electrochemical performance of cathode-supported cell	42
4.5.3 Durability test	46
CHAPTER V	50
5.1 Conclusions	50
5.2 Recommendations.....	51
REFERENCES	52
APPENDIX.....	59
APPENDIX A: Crystallite size	59
APPENDIX B: Lattice parameter.....	61
APPENDIX C: Tolerance factor	62
APPENDIX D: Activation energy of oxygen electrode for oxygen-oxidation reaction	64
APPENDIX E: Hydrogen production rate	65

APPENDIX F: Cell degradation rate..... 66

APPENDIX G: Thermal expansion coefficient of anode layer..... 66

VITA..... 67



LIST OF FIGURES

	Page
Figure 2.1 Schematic drawing of hydrogen production.....	5
Figure 2.2 Schematic drawing of ABO_3 perovskite structure showing the formation of A ion, B ion and oxygen atom in three-dimensional cubic lattice.....	9
Figure 2.3 Schematic drawing of the relationship of ionic radii in the perovskite structure	9
Figure 2.4 Oxygen permeation flux of doping W^{6+} on BSCF with 0, 0.1 and 0.3125mol% at 800°C. And the thickness of membranes is 1.0mm.....	11
Figure 2.5 Electrical conductivity of doping W^{6+} on BSCF with 0, 0.1 and 0.3125mol% in air between 500 and 900°C.....	12
Figure 2.6 XRD patterns of BSCFM after exposed for 14 days at 700°C in the pure hydrogen atmosphere. Triangle shows the position of the peaks of hexagonal phase.	12
Figure 2.7 Electrical conductivity of BSCFM in air. The inset shows the electrical conductivity with various dopant concentration.....	13
Figure 2.8 The ASR of the BSCFT composite with various amount of Ti^{4+} dopant compared to the ASR of Pt electrodes.....	14
Figure 2.9 Electrical conductivity of $BaCo_{0.7}Fe_{0.3-x}Nb_xO_{3-\delta}$ ($0.08 \leq x \leq 0.20$) in air.....	15
Figure 2.10 XRD patterns of $BaCo_{0.7}Fe_{0.3-x}Nb_xO_{3-\delta}$ before and after heat-treated in 5% H_2 and Argon at 900°C for 5h.	15
Figure 2.11 Electrical conductivity of BSCFN with various Sr^{2+} contents ($0.0 \leq x \leq 0.4$) in air.	16

- Figure 2.12** Oxygen permeation flux through partial substitution on A-site of BCFT: (1) La^{3+} -doped BCFT, (2) Sr^{2+} -doped BCFT, (3) Ca^{2+} -doped BCFT, (4) undoped BCFT at (a) 900°C and (b) 800°C in He..... 17
- Figure 2.13** Schematic drawing of particle diffusion on solid state reaction 18
- Figure 3.1** Ni-YSZ cathode preparation 22
- Figure 3.2** The conditions of calcination for BSCF and BSCFTa perovskite anode 25
- Figure 3.3** Schematic drawing of the test system 28
- Figure 4.1** XRD patterns of $\text{Ba}_{0.5}\text{Sr}_{0.5}(\text{Co}_{0.8}\text{Fe}_{0.2})_{1-x}\text{Ta}_x\text{O}_{3-\delta}$ (BSCFTa) where $x = 0, 0.05, 0.1, 0.15$ and 0.2 : (a) after calcined at 950°C for 4h; and (b) magnified scale at 2 Theta angles between 30° and 32.5° 30
- Figure 4.2** SEM images of $\text{Ba}_{0.5}\text{Sr}_{0.5}(\text{Co}_{0.8}\text{Fe}_{0.2})_{1-x}\text{Ta}_x\text{O}_{3-\delta}$ (BSCFTa) calcined at 950°C for 4h: (a) BSCFTa0.05, (b) BSCFTa0.10, (c) BSCFTa0.15, (d) BSCFTa0.20 and (e) BSCF 31
- Figure 4.3** EDX images of $\text{Ba}_{0.5}\text{Sr}_{0.5}(\text{Co}_{0.8}\text{Fe}_{0.2})_{1-x}\text{Ta}_x\text{O}_{3-\delta}$ (BSCFTa) find powder where $x = 0, 0.05, 0.1, 0.15$ and 0.2 which calcined at 950°C for 4h. 31
- Figure 4.4** TGA profile of $\text{Ba}_{0.5}\text{Sr}_{0.5}(\text{Co}_{0.8}\text{Fe}_{0.2})_{1-x}\text{Ta}_x\text{O}_{3-\delta}$ (BSCFTa), where $x=0, 0.05, 0.1, 0.15$ and 0.2 , in air and N_2 at temperature ranging from room temperature to 800°C 33
- Figure 4.5** The XPS spectra of $\text{Ba}_{0.5}\text{Sr}_{0.5}(\text{Co}_{0.8}\text{Fe}_{0.2})_{1-x}\text{Ta}_x\text{O}_{3-\delta}$ ($0 \leq x \leq 0.2$) powder: (a) Low resolution XPS scan, (b) O1s XPS spectra, (c) Co2p XPS spectra and (d) Fe2p XPS spectra 35
- Figure 4.6** Tolerance factor of $\text{Ba}_{0.5}\text{Sr}_{0.5}(\text{Co}_{0.8}\text{Fe}_{0.2})_{1-x}\text{Ta}_x\text{O}_{3-\delta}$ (BSCFTa), where $x = 0, 0.05, 0.1, 0.15$ and 0.2 with various valence state of Co and Fe metal ions at room temperature..... 38
- Figure 4.7** The EIS response: (a) impedance plot of the symmetrical half-cell with different Ta^{5+} -doping on BSCF at 600°C , inset is the summarize results from EIS curves; (b) impedance plot of half-cell with configuration of

BSCFTa0.10/YSZ/BSCFTa0.10 under various operating temperature in air, insert is the magnified image of EIS response at 700°C, 750°C and 800°C; and, (c) Arrhenius plot of temperature dependence of the ASR of the various Ta⁵⁺-doping on BSCF anode on YSZ electrolyte 42

Figure 4.8 The I/V response of Ni-YSZ/YSZ/Anode when the anode was BSCF, BSCFTa0.10 and LSM-YSZ, operated at 800°C under steam to H₂ ratio of 70:30 43

Figure 4.9 The I/V response of Ni-YSZ/YSZ/BSCFTa0.10: (a) Effect of operating temperature (steam to H₂ ratio of 70:30); (b) Effect of steam to H₂ ratio operating temperature at 800°C; and (c) The EIS response of Ni-YSZ/YSZ/BSCFTa0.10 in electrolysis (1.1v) and fuel cell mode (0.6v) under steam to H₂ ratio of 70:30 at 800°C, inset is the summarize results from fitted EIS curves..... 45

Figure 4.10 Single cell potential monitoring under electrolysis mode for 80h. (0.45A·cm⁻², 800°C and steam to H₂ ratio of 70:30) of Ni-YSZ/YSZ/LSM-YSZ, Ni-YSZ/YSZ/BSCF and Ni-YSZ/YSZ/BSCFTa0.10 47

Figure 4.11 Comparing electrochemical performance before and after operated under electrolysis mode for 80h. (0.45A·cm⁻², 800°C and steam to H₂ ratio of 70:30): (a)The I/V response of Ni-YSZ/YSZ/BSCF, Ni-YSZ/YSZ/BSCFTa0.10 and Ni-YSZ/YSZ/LSM-YSZ; (b) The magnified scale I/V response of Ni-YSZ/YSZ/BSCF and Ni-YSZ/YSZ/LSM-YSZ; and (c) The EIS response 48

Figure 4.12 SEM images of BSCF and BSCFTa0.10 anode after durability test under electrolysis mode for 80h. (0.45A·cm⁻², 800°C and steam to H₂ ratio of 70:30): (a), (b) and (c) illustrate the cross-section of Ni-YSZ/YSZ/BSCF, Ni-YSZ/YSZ/BSCFTa0.10 and Ni-YSZ/YSZ/LSM-YSZ cell, respectively; (d), (e) and (f) illustrate the magnified scale of cross-section of cell between BSCF and YSZ layer, BSCFTa0.10 and YSZ layer and LSM-YSZ and YSZ layer, respectively..... 49

LIST OF TABLES

	Page
Table 2.1 Activation energy of conductivity for BSCFM oxides in the temperature range of 30 to 400°C	13
Table 3.1 Chemicals for synthesis of perovskite anode.....	20
Table 3.2 Chemicals for cathode and electrolyte preparation	21
Table 3.3 Compositions of electrolyte material	23
Table 3.4 The components of all anode	23
Table 3.5 Steam to H ₂ ratio of operating condition.....	28
Table 4.1 The stoichiometry of Ba _{0.5} Sr _{0.5} (Co _{0.8} Fe _{0.2}) _{1-x} Ta _x O _{3.δ} (0 ≤ x ≤ 0.2) anode calculated from EDX analysis.....	32
Table 4.2 The area of the XPS peaks representing different kinds of oxygen species	36
Table 4.3 The area of the XPS peaks representing different kinds of Co ions and the ratio of Co ³⁺ /Co ⁴⁺ in Ba _{0.5} Sr _{0.5} (Co _{0.8} Fe _{0.2}) _{1-x} Ta _x O _{3.δ} (0 ≤ x ≤ 0.2).....	37

CHAPTER I

INTRODUCTION

1.1 Motivation

Traditional power generation based on natural gas, coal and petroleum are mainly causes of the serious environmental such as air and water pollution. All human activities depend on these energy resource that affects the ecosystem, including the water, air and the life. The result is a web of harmful impacts from overloading with carbon dioxide (CO_2) accumulation on our atmosphere to the greenhouse gas emissions. Thus, an alternative energy which is clean energy has been worldwide interest.

In 1992, hydrogen is considered an alternative fuel on the Energy Policy Act (EPAAct)[1]. It is a potential resource for clean vehicles. Furthermore, electricity generation, heating and industrial processes. In general, hydrogen can be produced from natural gas and hydrocarbon through several methods such as steam reforming, coal gasification and petroleum coke. However, these processes can be produced its major by-product in carbon emission. Moving away from hydrocarbon as a fuel, solid oxide electrolysis cell (SOEC) is a promising technology and feasible to the zero emission and also use as a non-depleted resource which can be renewable.

Solid oxide electrolysis cell includes an electrolyte, porous solid ceramic cathode and anode. It is an alternative method for hydrogen production through steam electrolysis operating at high temperature with high purity of hydrogen without purification unit. Additionally, SOEC is able to produce syngas hydrogen and carbon monoxide ($\text{H}_2 + \text{CO}$) from electrolysis of water and carbon dioxide ($\text{H}_2\text{O} + \text{CO}_2$) which can be further used for the production of fuel [2]. The challenge of SOEC is still limited by poor electrocatalytic activity at the anode, leading to a lower oxygen permeation reaction. Perovskite anode offers fast kinetics and high efficiency with the general formula of ABO_3 . The crystal perovskite structure consists of A and B site,

where A site is either rare earth or alkaline earth and B site can be transition metal. For the conventional perovskite materials used as anode in SOEC, the A site usually La, Ba and Sr, while the B site usually Mn, Co and Fe [3]. Among the several types of anode perovskite, cobalt based mixed conducting oxides have been widely investigated as an oxygen electrode, especially $\text{SrCo}_{0.8}\text{Fe}_{0.2}\text{O}_{3.8}$ (SCF), which show the high performance on oxygen permeability at intermediate temperature, but has rather limited structural stability in reducing temperature [4]. To improve this material, SCF can be developed by partial substituting Sr with Ba because the Ba^{2+} cation has a much greater covalent bond on the perovskite structure [5]. Normally, the stability of crystal structures is indicated by Goldschmidt tolerance factor (t). It is the relationship between the radii of the various ions. The ideal perovskite is the cubic structure with the tolerance factor close to 1.0 at high temperature. The cubic perovskite structure is stable in the range of $0.80 < t < 1.0$ [6, 7]. However, the composition $\text{Ba}_{0.5}\text{Sr}_{0.5}\text{Co}_{0.8}\text{Fe}_{0.2}\text{O}_{3.8}$ (BSCF) still suffer from oxidation instability of Co^{2+} for long term operation specially under high temperature electrolysis, resulting in the tolerance factor of BSCF varies within $0.97 < t < 1.07$ [6]. To provide a better structure stability, partial substitution of highly charge cations on BSCF structure is related to the mechanism of charge compensation. First, a valence reduction on B-site under high temperature can occur - the valence of Co^{4+} and Fe^{4+} reduces to Co^{3+} or Co^{2+} and Fe^{3+} , respectively. After that, the lattice parameter increases, leading to an increasing oxygen vacancies. Second, the high-charge cation which is the fixed valence state at high temperature can stabilize the charged cation on B-site. The excess of positive charge attracts the electron density from Co, resulting in an increase of positive charges on Co as a consequence of reduce the lattice parameter and lower the concentration of oxygen vacancies, which result in stabilize the BSCF structure. Therefore, in this study partial substitute BSCF on B-site (Co/Fe) with adequate transition metal has been investigated in term of phase stability while maintaining its electrochemical performance as an oxygen electrode.

1.2 Research objectives

To compare the electrochemical performance of SOEC anodes and prepare $\text{Ba}_{0.5}\text{Sr}_{0.5}(\text{Co}_{0.8}\text{Fe}_{0.2})_{1-x}\text{Ta}_x\text{O}_{3.8}$ by a partial substitution of barium strontium cobalt ferrite (BSCF) on B-site with Ta^{5+} .

Subobjective includes:

1.2.1 To compare the electrochemical performance and durability of selected anodes.

1.2.2 To synthesize oxygen electrode powder with a partial substitution of BSCF on B-site with highly charged cations (Ta^{5+}).

1.2.3 To investigate the effect of the amounts of Ta^{5+} dopant on the performance of perovskite anode.

1.3 Research scopes

1.3.1 Single phase perovskite of $\text{Ba}_{0.5}\text{Sr}_{0.5}\text{Co}_{0.8}\text{Fe}_{0.2}\text{O}_{3.8}$ (BSCF) and $\text{Ba}_{0.5}\text{Sr}_{0.5}(\text{Co}_{0.8}\text{Fe}_{0.2})_{1-x}\text{Ta}_x\text{O}_{3.8}$ (BSCFTa) ($x = 0.05, 0.1, 0.15$ and 0.2% mol) are synthesized by citrate-EDTA complexing method.

1.3.2 Comparing basic oxygen electrodes including lanthanum strontium manganite-yttria stabilized zirconia (LSM-YSZ) and BSCF with BSCFTa electrode.

1.3.3 For single cell, nickel-yttria stabilized zirconia (Ni-YSZ) and 8%mol yttria-stabilized zirconia (YSZ) are used for cathode and electrolyte layer, respectively.

1.3.4 An area of bottom cell is 2.54 cm^2 . The cell is fabricated by mold and press and circular area of oxygen electrode is 0.19 cm^2 , depositing by screen printing with doctor blade.

1.4 Expected benefit

In this research, various amount of Ta^{5+} dopant in BSCF perovskite structure will be investigated for hydrogen production from steam electrolysis using solid oxide electrolysis cell. The studies on SOEC based on cell assemblies composed of Ni-YSZ cathode/ YSZ electrolyte/ varied anodes. The anode in this study includes LSM-YSZ a basic anode, BSCF and BSCFTa.

The outcome of this study is newly developed BSCFTa anode, which is expected to improve the performance stability of the perovskite anode in SOEC.

Green hydrogen will be produced through high-temperature steam electrolysis using SOEC and eventually encourages the decarbonisation of energy consumption.



CHAPTER II

THEORY

2.1 SOEC

2.1.1 Principle of operation

Solid oxide electrolysis cell (SOEC) is a reversely operated of solid oxide fuel cell to produce hydrogen and oxygen. It is a device that achieve the electrolysis of water by fed steam and applied electrical into the porous cathode, then water molecules diffuse to the reaction sites and dissociate to form hydrogen gas and oxygen ions. Hydrogen gas diffuses to the cathode site and oxygen ions pass through dense electrolyte to the anode as an oxygen electrode. After that, the oxygen ions is oxidized to oxygen gas, as shown in Fig. 2.1.

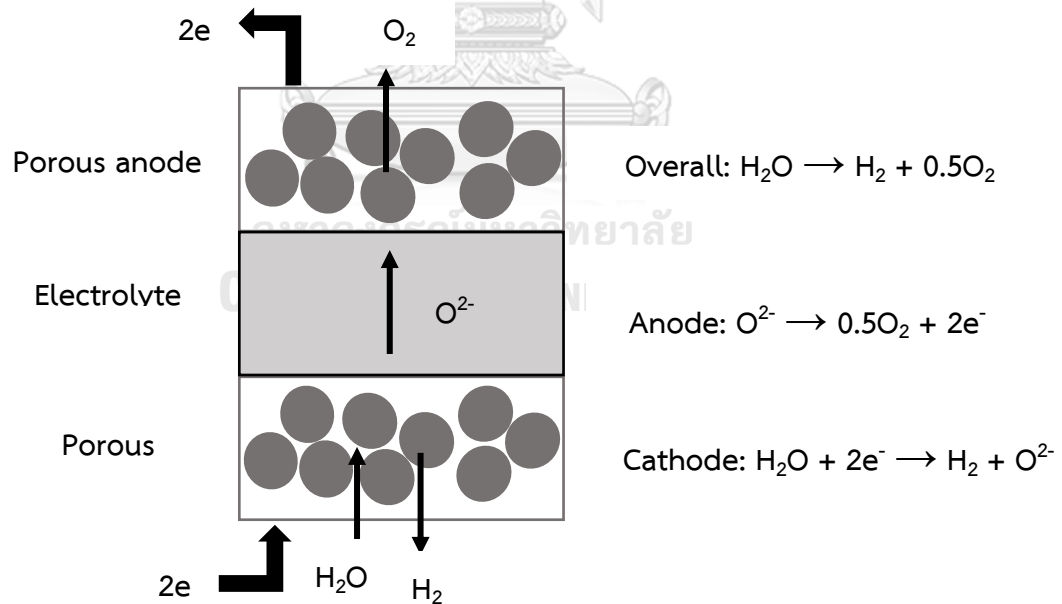


Figure 2.1 Schematic drawing of hydrogen production

2.1.2 SOEC component requirements

2.1.2.1 Electrolyte materials

Yttria-stabilized zirconia (YSZ, $Y_2O_3-ZrO_2$) is the most widely used materials as solid electrolyte in SOEC because of its high ionic and low electronic conductivity. YSZ is adopts from cubic fluorite structure to form cubic polymorph to stabilize the ZrO_2 cubic fluorite at lower temperature and increase the ionic conductivity. The highest ionic conductivity is $13 \times 10^{-2} S \cdot cm^{-1}$ at $1000^\circ C$, when adding 8mol% Y_2O_3 into the host ZrO_2 [8]. And the thermal expansion coefficient (TEC) of YSZ is $10.6-11.0 \times 10^{-6} k^{-1}$ [9].

2.1.2.2 Cathode materials

The most common cathodes are composite materials, consisting of a metallic component mixed with the electrolyte composition. The metallic component acts as electronic conductor, while the electrolyte provides the good match in thermal expansion between cathode and electrolyte layer. Pure metal catalyst such as nickel is an excellent electrode for hydrogen oxidation due to good porosity features for transport of carrier gases [10]. The thermal expansion coefficient of Ni is $13.3 \times 10^{-6} k^{-1}$. It shows the thermal compatibility between Ni and YSZ electrolyte [10], which improving the durability for long-term operation.

2.1.2.3 Anode materials

The anode is required to be a permeable structure at high operating temperature and generate high oxygen ion and electronic conductivity. To obtain good oxygen ion conductivity, an anode can be achieved by these requirements such as containing the suitable amount of oxygen vacancies, which are the carriers of oxygen ion charge in perovskite oxide and having their porosity application [11]. To complete these requirements, perovskite oxides structure is usually used as anode materials for SOEC due to mixed oxides in perovskite structure showing large number of oxygen ion pathways and generating strong combination of ionic and electronic conductivity. There are many mixed perovskite oxides that used at present such as

lanthanum strontium manganite (LSM), lanthanum strontium manganite-yttria stabilized zirconia (LSM-YSZ), lanthanum strontium cobalt ferrite (LSCF) and barium strontium cobalt ferrite (BSCF), are described as below

LSM is a traditional anode material that used in SOEC. It adopts LaMnO_3 , which is neither good electrical conductor nor good catalyst for oxygen reduction by doping LaMnO_3 on La site with Sr to form $\text{La}_{0.8}\text{Sr}_{0.2}\text{MnO}_{3-\delta}$. Doping LaMnO_3 shows increasing the electronic conductivity because it increases the electron-hole concentration when increasing Sr concentration [12].

LSM-YSZ is an anode composite, which is a composite of LSM and YSZ material. It provides a good compatibility of interface between YSZ electrolyte and LSM-YSZ anode because the thermal expansion behaviour of LSM-YSZ anode is close to the typical YSZ electrolyte [13].

LSCF and BSCF are mixed electronic and ionic conductor (MIEC) as they display both high electronic and fast ionic conductivity. The ability of cobalt in the perovskite structure is easily to alter their oxidation state and follow by formation of oxygen vacancies. However, a large amount of cobalt and oxygen vacancies results in high TEC that affect to the mismatching with the electrolyte, followed by poor stability in long-term operation.

For LSCF, $\text{La}_{0.6}\text{Sr}_{0.4}\text{Co}_{0.2}\text{Fe}_{0.8}\text{O}_{3-\delta}$ is the most composition which is used in SOEC. It has a large TEC of $15.3 \times 10^{-6} \text{ k}^{-1}$ at 100-600°C. Therefore, its TEC is largely different from that of common YSZ electrolyte, resulting in incompatibility between interface of YSZ and LSCF. However, it has been reported that gadolinium doped ceria (GDC) is the commonly electrolyte that properly used with LSCF because of similarity in TEC [14].

For BSCF, the cobalt rich BSCF ($\text{Ba}_{0.5}\text{Sr}_{0.5}\text{Co}_{0.8}\text{Fe}_{0.2}\text{O}_{3-\delta}$) perovskite is a recently developed. BSCF is improved from $\text{SrCo}_{0.8}\text{Fe}_{0.2}\text{O}_{3-\delta}$ (SCF) by partial replacement of Sr^{2+} with Ba^{2+} to offer the ionic conductivity and suppress the phase stability. The BSCF has great attention as an oxygen electrode due to it good in

catalyst for oxidation reduction, high current density and, also very small polarization resistance, approximately $0.071 \Omega \cdot \text{cm}^2$ at 600°C [15]. Nevertheless, it still suffers from phase instability from cubic to hexagonal structure when operate temperature below 900°C [16]. Hence, to provide a good phase stability, while maintaining its electrochemical performance of BSCF should be optimized.

2.2 Structure of perovskites

One of a large group of compounds are perovskites. Their structure are similar to calcium titanium oxide (CaTiO_3), which is crystal structure of the natural mineral and it was discovered by the Russian mineralogist Perovski in 1839 and considered to be the origin of perovskite structure [17]. There are many kinds of crystals which have the same structure in perovskites such as oxides, nitrides and halides. However, the perovskite oxides are the most interesting because they have ionic and electronic conducting properties.

2.2.1 Crystal structure

ABO_3 is the common formula for perovskite, they are very popular as SOEC anode. In this formula, A-site is a larger cation such as rare earth or alkaline earth, while B-site is a small cation such as transition metal. The structure of perovskite structure has cubic symmetry. Each of corner shares BO_6 octahedra with the A cation located at center, twelve-fold coordinate and the B cation is six-fold coordinated surround by an octahedron, as shown in Fig. 2.2. Alternately, A cation and B cation are in the middle position of the cube and the octahedron, respectively.

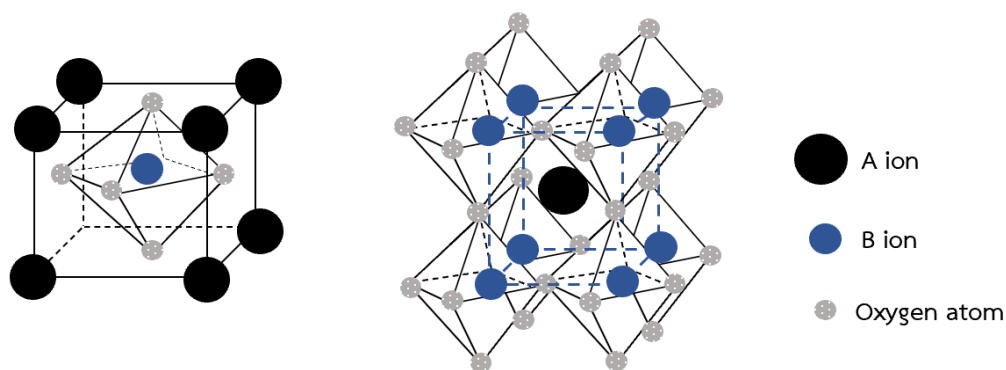


Figure 2.2 Schematic drawing of ABO_3 perovskite structure showing the formation of A ion, B ion and oxygen atom in three-dimensional cubic lattice.

2.2.2 Tolerance factors in perovskites

In this perovskite structure, the size and coordinated preference of ions need to be satisfied simultaneously. The accommodate perfectly of crystal structure can indicated by Goldschmidt tolerance factor (t). It is the relationship between the radii of the different ions. In the ideal cubic unit cell structure, where the atoms are associating to each other, the B-O (r_B+r_O) and A-O (r_A+r_O) distance are equal to $a/2$ (a is the cubic unit cell parameter) and $\sqrt{2}/2$, respectively. Then, degree of the deviation from the cubic structure is committed by the tolerance factor. The relationship of ionic radii in the perovskite structure, as shown in Fig. 2.3 and Eq. (2.1) to (2.4), respectively.

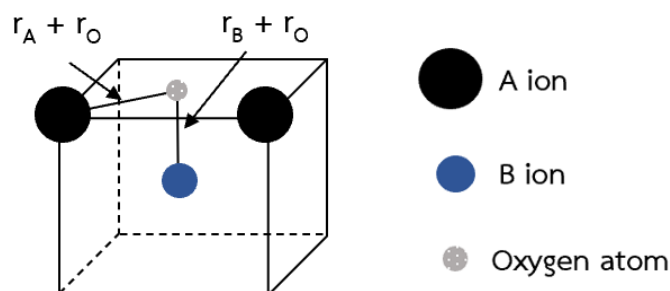


Figure 2.3 Schematic drawing of the relationship of ionic radii in the perovskite structure

$$a = 2x_B \cdot r_O = 2(r_B + r_O) \quad (2.1)$$

and
$$a = \frac{1}{\sqrt{2}} \cdot 2x_A \cdot r_O = \sqrt{2}(r_A + r_O) \quad (2.2)$$

Hence,
$$2x(r_B + r_O) = \sqrt{2}x(r_A + r_O) \quad (2.3)$$

$$t = \frac{r_A + r_O}{\sqrt{2}(r_B + r_O)} \quad (2.4)$$

2.2.3 Non-stoichiometry in perovskites

Non-stoichiometric compounds are chemical compounds diverged from stoichiometry that cannot be displayed by a ratio of defined natural number. Most of the nonstoichiometric compounds are transition metal oxide which is a part of B-site in general formula, $ABO_{3-\delta}$ in perovskite structure [18]. Normally, non-stoichiometry in perovskite can arise from oxygen deficiency ($ABO_{3-\delta}$), cation deficiency at A-site ($A_{1-\delta}BO_3$) and cation deficiency at B-site ($AB_{1-\delta}O_3$). For the oxygen deficiency, the characteristics of A and B cation such as size and coordination number are important. Oxygen vacancies are accomplished by replacing ions of similar magnitude but having various valence. For example, replacement of La^{3+} in $LaBO_3$ with Sr^{2+} to form $La_{1-x}Sr_xBO_{3-\delta}$, then oxygen vacancies are generated in the structure. For the cation deficiency, A-site cation can be partially missing because the arrangement in BO_3 forms a very suitable network for stability purpose, while B-site vacancies rarely found because of the high cation which leads to the small size [19].

2.3 Metal doping at A and B site of BSCF

BSCF perovskite material shows better oxygen permeability at high temperatures range. However, several works of literature found that BSCF suffers from Co content because of its greater ability to change the valence from Co^{2+} to Co^{3+} or Co^{4+} when operated at high temperature [6]. Then, the lowering on ionic radius of B-site leads to decrease the stability and lower performance due to shrinkage of BSCF perovskite structure. To improve the BSCF that is used as an

oxygen electrode, the doping elements on A-site such as gadolinium increase the oxygen vacancies, which affects the oxygen permeability and electrical conductivity [20]. And doping element on B-site such as tungsten (W), molybdenum (Mo), titanium (Ti), niobium (Nb) and tantalum (Ta), which affect to the structural stability of perovskite are described as below.

2.3.1 W-doped BSCF

The effect of doping W^{6+} on BSCF was investigated by Zhang et al [21]. The doping amount is varied between 0 and 0.3125mol% of W^{6+} . It is reported that the oxygen permeation flux of BSCFW0.3125 has the most stable oxygen permeation flux at 800°C during 100h of the testing period under air and helium atmosphere, as shown in Fig. 2.4. The stability of perovskite depends on the oxygen vacancies content and Lewis acidity. The BSCFW0.3125 with high Lewis acidity decreases the oxygen vacancies, which is the main cause for increasing the stability of perovskite materials.

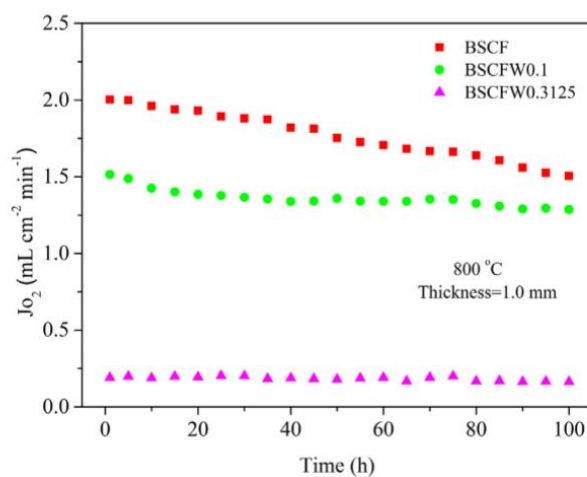


Figure 2.4 Oxygen permeation flux of doping W^{6+} on BSCF with 0, 0.1 and 0.3125mol% at 800°C. And the thickness of membranes is 1.0mm.

Conversely, the increase in the amount of W^{6+} dopant in BSCF, a lowering in electrical conductivity is shown in Fig 2.5. For example, the maximum conductivity

under air condition of BSCF is approximately $50 \text{ S}\cdot\text{cm}^{-1}$, while the BSCF doped with 0.1 and 0.3125mol% of W^{6+} are 35 and $3 \text{ S}\cdot\text{cm}^{-1}$, respectively.

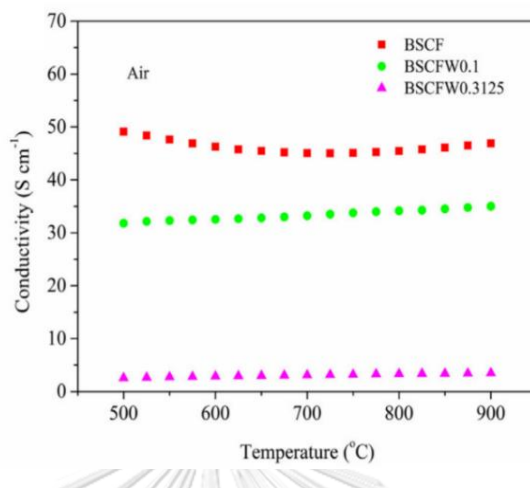


Figure 2.5 Electrical conductivity of doping W^{6+} on BSCF with 0, 0.1 and 0.3125mol% in air between 500 and 900°C.

2.3.2 Mo-doped BSCF

The effect of doping Mo^{6+} on BSCF was investigated by Shubnikova et al [22]. Phase stability of BSCFM is studied by varying amounts of Mo^{6+} doping between 0 and 15mol%. The test is carried out for 14 days at 700°C in pure hydrogen atmosphere (oxidizing condition), as shown in Fig. 2.6. It is found that 2mol% of Mo^{6+} doping on BSCF is sufficient to avoid the transition from cubic to hexagonal phase.

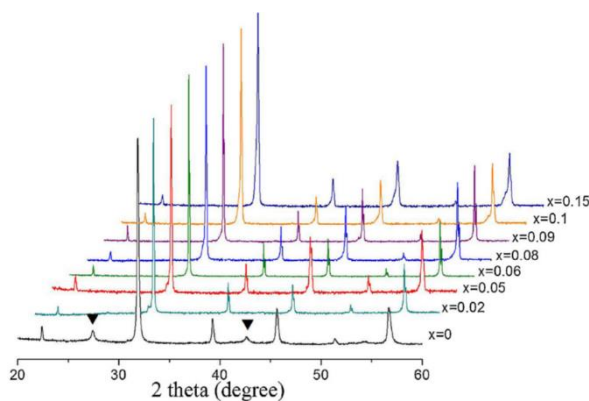


Figure 2.6 XRD patterns of BSCFM after exposed for 14 days at 700°C in the pure hydrogen atmosphere. Triangle shows the position of the peaks of hexagonal phase.

In term of electrical conductivity of BSCFM oxides in air, as shown in Fig. 2.7. The conductivity of all samples increase with increasing temperature up to 600°C, and then decreases with further increasing temperature. In the inset of Fig. 2.7, the conductivity of BSCFM ($0.06 < x < 0.1$) in the temperature at 600 and 650°C is shown. The conductivity value is more than the undoped BSCF. These contradicting results with the general study is explained by that the substitution of B-site by higher cations in perovskite structure results in decreasing the conductivity because of lowering in the oxygen vacancies. These results may be related to the formation of a composite which takes place in BSCFM that has a nanostructuring, then produces the superior performance phase. And the value of activation energy (E_a) of BSCFM ($0 \leq x \leq 0.15$) in 30-400°C are in the range of 0.30-0.37 eV, as shown in Table 2.1

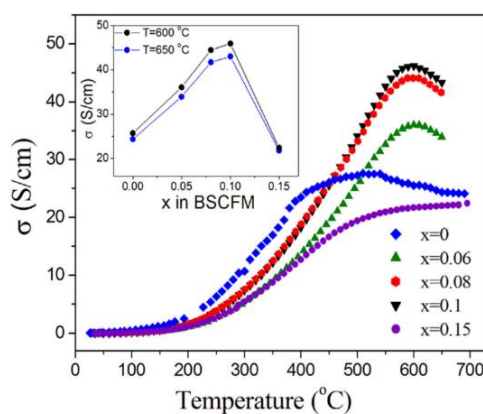


Figure 2.7 Electrical conductivity of BSCFM in air. The inset shows the electrical conductivity with various dopant concentration.

Table 2.1 Activation energy of conductivity for BSCFM oxides in the temperature range of 30 to 400°C

Replacing, x in BSCFM	E_a (eV)
0	0.30
0.06	0.38
0.08	0.38
0.1	0.37
0.15	0.37

2.3.3 Ti-doped BSCF

The effect of doping Ti^{4+} on B-site of BSCF is shown in Fig. 2.8 [23]. The Arrhenius plot of area specific resistance (ASR) of the oxygen electrode with varying the content of Ti^{4+} between 0 and 10mol% is compared to the Pt electrode. It can be seen that the ASR increases with the increasing of Ti^{4+} content and Ti^{4+} has slightly effects on the E_a . The E_a increases from 0.81eV for the undoped BSCF to 0.86 eV for 10mol% of Ti^{4+} on BSCF, which are smaller than the E_a of Pt electrode. The increase of ASR and E_a with increasing the amount of Ti^{4+} content related to a decline in the catalytic activity due to the reaction of oxygen reduction induced by the partial replacement of Ti^{4+} on B-site of on BSCF.

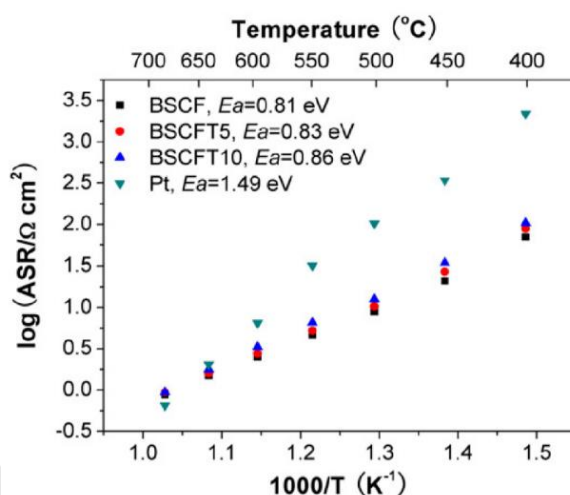


Figure 2.8 The ASR of the BSCFT composite with various amount of Ti^{4+} dopant compared to the ASR of Pt electrodes.

2.3.4 Nb-doped BSCF

The effect of doping Nb^{5+} on $\text{BaCo}_{0.7}\text{Fe}_{0.3-x}\text{Nb}_x\text{O}_{3.8}$ (BCF) with A-site fully occupied by Ba was investigated by Cheng et al [24]. They study in the conductivity of BCFN with the various amount of Nb^{5+} from 0.08 to 0.20 in air is shown in Fig. 2.9. The electrical conductivity increases with increasing temperature and decreases with the Nb^{5+} substitution content on B-site (Fe) of BCF. However, Nb-doping can enhance good structural stability of BCFN in reducing temperature, as shown in Fig. 2.10. After

heat-treated, the lattice structure of 8mol% Nb is distorted due to the peak width becomes larger. So, the dopant of 20mol% Nb on BCF is more stable than 8mol% Nb.

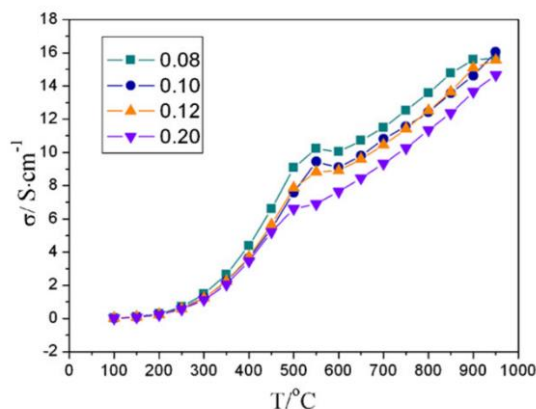


Figure 2.9 Electrical conductivity of $\text{BaCo}_{0.7}\text{Fe}_{0.3-x}\text{Nb}_x\text{O}_{3.6}$ ($0.08 \leq x \leq 0.20$) in air.

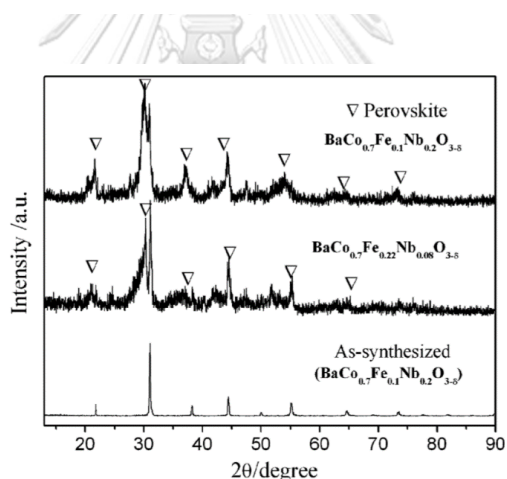


Figure 2.10 XRD patterns of $\text{BaCo}_{0.7}\text{Fe}_{0.3-x}\text{Nb}_x\text{O}_{3.6}$ before and after heat-treated in 5% H_2 and Argon at 900°C for 5h.

Moreover, the effect of partial substitution of Sr on $\text{Ba}_{1-x}\text{Sr}_x\text{Co}_{0.7}\text{Fe}_{0.2}\text{Nb}_{0.1}\text{O}_{3.6}$ (BSCFN) was investigated by Li et al [25]. The conductivity of BSCFN with varying amounts of Sr between 0 and 0.4mol% by fixed 0.1mol% of Nb is investigated and shown in Fig. 2.11. The electrical conductivity increases with increasing Sr content, while the E_a values slightly decrease.

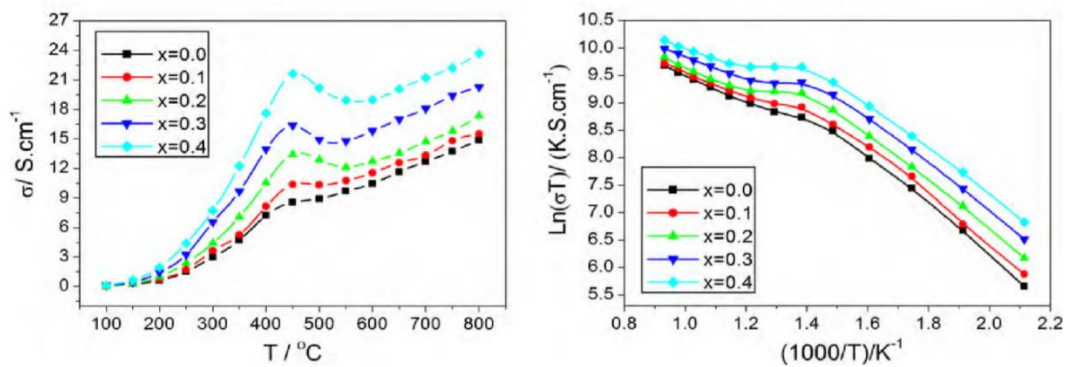


Figure 2.11 Electrical conductivity of BSCFN with various Sr^{2+} contents ($0.0 \leq x \leq 0.4$) in air.

2.3.5 Ta-doped BSCF

Ta^{5+} is one of the interesting elements for partial substitution on the B-site (Co/Fe) of BSCF perovskite because it has a higher cation, which leads to a valence reduction on B-site from Co^{4+} to Co^{3+} or Co^{2+} as a consequence of decrease the concentration of oxygen vacancies on B-site (Co/Fe) and stabilize the BSCF structure [6]. Furthermore, it has similar ionic radii with Nb^{5+} (0.078 nm) and also better than Nb^{5+} such as Ta-O bond is stronger than Nb-O bond, the electronegativity of Ta^{5+} is lower than Nb^{5+} leads to lower valence of cobalt and more oxygen vacancies. And the TEC of Ta_2O_5 that used as reagent is lower than Nb_2O_5 , resulting in the greater performance of BSCF perovskite materials [25].

Oxygen permeation flux is one of the parameters that indicates the performance of BSCF perovskite. The partial substitution on Ba^{2+} of $\text{BaCo}_{0.7}\text{Fe}_{0.225}\text{Ta}_{0.075}\text{O}_{3.6}$ (BCFT) with Ca^{2+} , La^{3+} and Sr^{2+} was investigated by Bo et al. [3], as shown in Fig. 2.12. At 900°C , it shows that the stabilities of BLCFT, BSCFT, BCCFT and BCFT are nearly constant for 1,400 minutes. And at 800°C , the oxygen permeation stabilities are lower than the operation at 900°C . And for Sr^{2+} dopant on BCFT into BSCFT, the oxygen permeation flux performance between 0 and 1,400 minutes at 900°C are nearly 2.0 ml/min cm^2 and for 800°C , the performance reduces from 1.4 to 1.3 ml/min cm^2 .

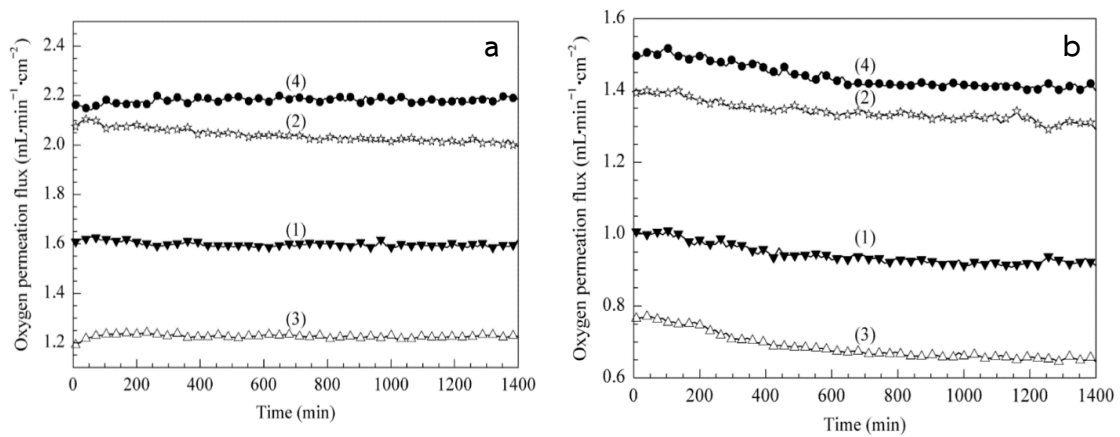


Figure 2.12 Oxygen permeation flux through partial substitution on A-site of BCFT: (1) La³⁺-doped BCFT, (2) Sr²⁺-doped BCFT, (3) Ca²⁺-doped BCFT, (4) undoped BCFT at (a) 900°C and (b) 800°C in He

2.4 Perovskite synthesis

2.4.1 Solid state reaction

Solid state reaction is the easiest method for perovskite oxide synthesis because it is very convenient and simple method. It involves the ball mill mixing powders of oxide or carbonates, then high temperature calcination to complete the reaction. The reaction during mixing the raw materials react at the interface of the mixed solids [26], shows in Fig 2.13. However, this method introduced the impurities from raw materials and made the multiple phases that affect to the performance of perovskite. And the particle size and wide range particle distribution of finished powder are also the limitations of this method.

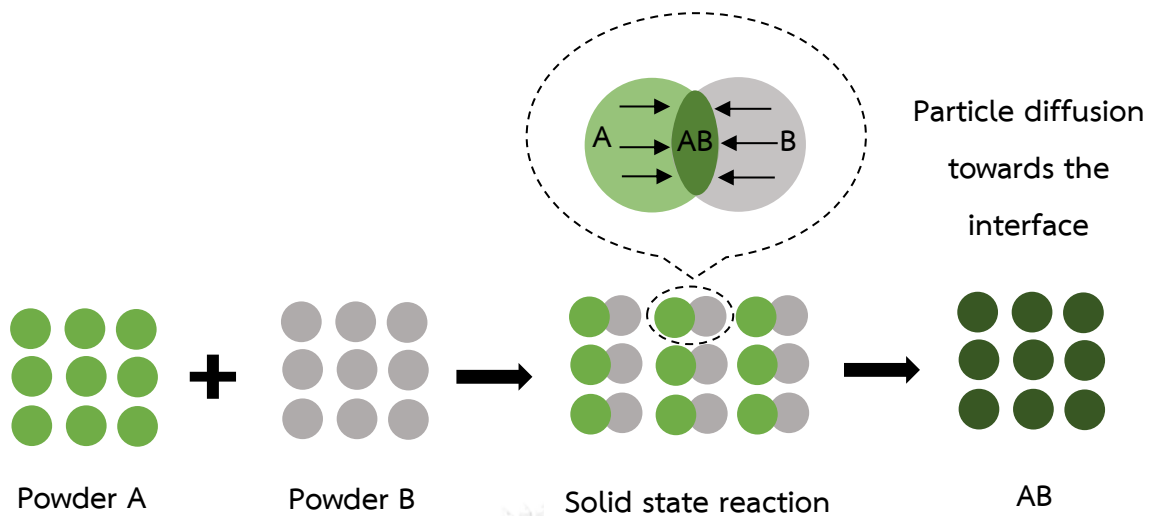


Figure 2.13 Schematic drawing of particle diffusion on solid state reaction

2.4.2 Wet chemical synthesis

Wet chemical synthesis is a conventional way for perovskite materials synthesis. Since it can exhibit a homogeneous and single-phase perovskite under the high temperature. There is various route can be used to synthesize perovskite such as solution combustion, co-precipitation, or citrate-EDTA method, are described as below

2.4.2.1 Solution combustion

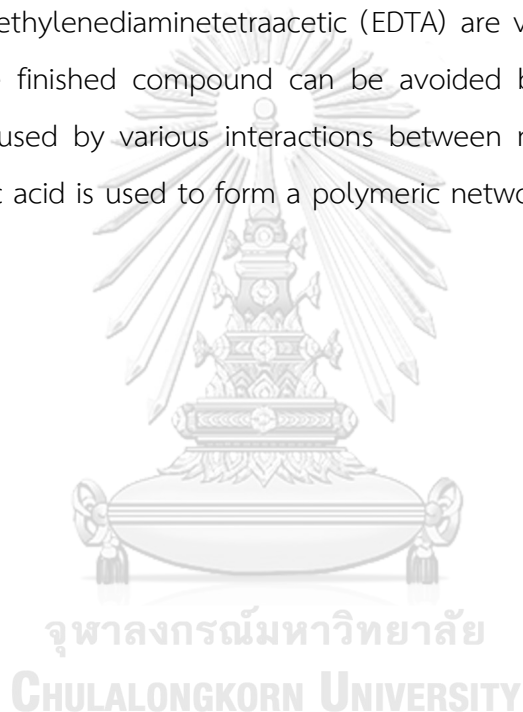
The solution combustion method uses a mixing of metal nitrates and aqueous solution such as urea, glycine or water-soluble carbohydrates. This method obtained the finished product directly after using the combustion. The advantage of the solution combustion method are low operating temperature and having an improved controllable particle size of the finished product [27].

2.4.2.2 Co-precipitation

The requirement of Co-precipitation is a supersaturation condition where metal cations solution is combined with the precipitation agent. The final products which is pure and good homogeneity are obtained. Nevertheless, formation of co-precipitated powder takes a long time because of the slow precipitation.

2.4.2.3 Citrate-EDTA complexing method

Citrate-EDTA complexing method is an improved sol-gel technique with more controllable in the particle size and the dopants spread uniformly in the finished product. It involves a chemical solution reacts with powders of metal alkoxides, metal chlorides or metal nitrate to produce colloidal particle (sol) through hydrolysis and polycondensation reaction. Then, the sol becomes an inorganic network with having a liquid phase (gel), followed by heat treatment to remove solution and calcination to obtain the final products. In this method, a complexation of citric acid and ethylenediaminetetraacetic (EDTA) are very important. The partial segregation in the finished compound can be avoided by using chelating agents, which may be caused by various interactions between metal ions present in the solution. And citric acid is used to form a polymeric network from polycondensation reaction [28].



CHAPTER III

EXPERIMENTAL

The experimental procedures including processing of cathode and electrolyte preparation, perovskite anode powder synthesis, solid oxide electrolysis cell fabrication and characterization of materials, are described as below:

3.1 Chemicals

Table 3.1 Chemicals for synthesis of perovskite anode

Reagents	Formula Weight	%Purity	Company
Ba(NO ₃) ₂	261.34	99.0	Himedia
Sr(NO ₃) ₂	211.63	99.0	Sigma-Aldrich
Co(NO ₃) ₂ ·6H ₂ O	291.03	99.99	Sigma-Aldrich
Fe(NO ₃) ₃ ·9H ₂ O	404.00	98.0	Sigma-Aldrich
Ta ₂ O ₅	441.89	99.0	Sigma-Aldrich
EDTA C ₁₀ H ₁₆ N ₂ O ₈	292.24	98.0	Vetec
Citric acid monohydrate C ₈ H ₈ O ₇ ·H ₂ O	210.14	99.5	Merck
NH ₃ H ₂ O	35.05	25	Merck
HNO ₃	63.01	65	Merck

Table 3.2 Chemicals for cathode and electrolyte preparation

Reagents	%Purity	Company
NiO	99.0	Sigma-Aldrich
$(Y_2O_3)_{0.08}(ZrO_2)_{0.92}$ (YSZ)	-	Kceracell
$La_{0.8}Sr_{0.2}Mn_{1.02}O_3$ (LSM)	-	Kceracell
Ethanol	Absolute	Merck
Xylene	98.5	Sigma-Aldrich
Butyraldehyde	96.0	Sigma-Aldrich
Polyethyleneglycol (PEG)	50	Sigma-Aldrich
Polyvinyl butyral resin (butar98)	-	Sigma-Aldrich
Polyvinylpyrrolidone (PVPD)	-	Sigma-Aldrich
Alpha terpineol (Binder)	-	Sigma-Aldrich

3.2 Cathode preparation

Ni-YSZ was used in this investigation. The difference size between NiO and YSZ powder was control at 1-1.5 times. Ni and YSZ powder were mixed in a weight ratio of 60:40 by ball-milling for 1 day using ethanol as the media. Then, ethanol was removed by baking at 110°C for 24 h. After that, 3g of mixed powder was pressed into pellets for 30s under 1,500 psi. Finally, the green disc was sintered at 1,100°C for 2 h. to obtain a button cathode. Flow chart of cathode preparation is shown in Fig.3.1

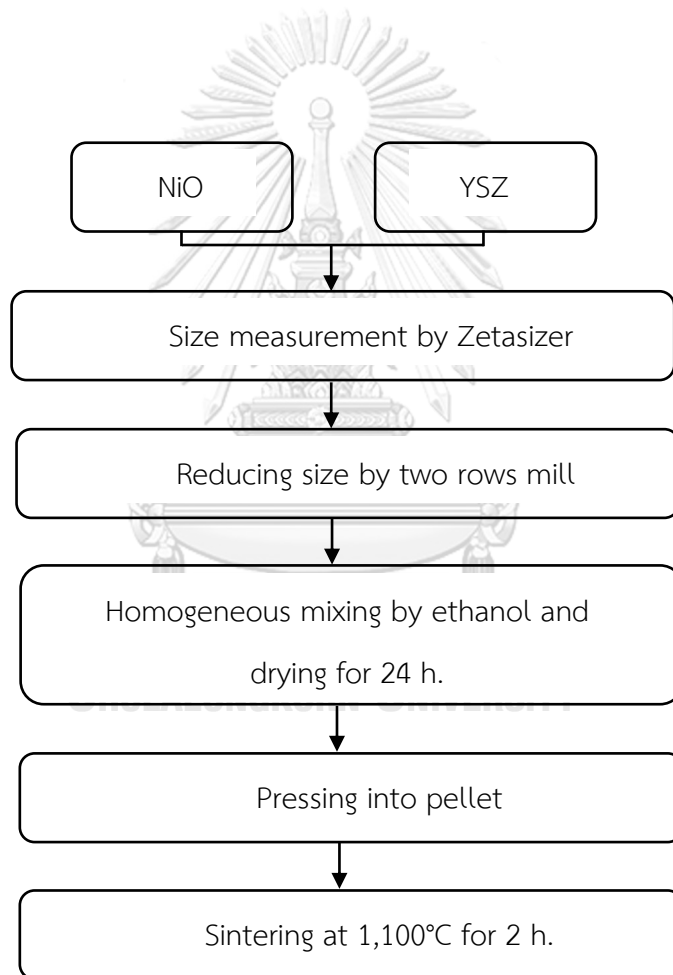


Figure 3.1 Ni-YSZ cathode preparation

3.3 Electrolyte preparation

The compositions of electrolyte materials are presented in Table 3.3. After that, the mixture was stirred for 1 h. and heated at 70°C, the YSZ slurry was formed.

Table 3.3 Compositions of electrolyte material

YSZ (g)	Solvent system		Polyvinyl butyral resin (g)	Polyethylene glycol (g)	Polyvinyl pyrrolidone (g)
	Xylene (ml)	Butyraldehyde (ml)			
10	36.3	11	0.3	0.002	0.5

3.4 Synthesis of perovskite anode powder by citrate-EDTA complexing method

Composition of Ta doped BSCF is presented in Table 3.4. Different amount of Ta (0.05-0.20 moles) was doped in to BSCF structuring by replacing B site which are Co and Fe.

Table 3.4 The components of all anode

Doping	Replacing	Anode	Abbreviation
-	-	$Ba_{0.5}Sr_{0.5}Co_{0.8}Fe_{0.2}O_{3-\delta}$	BSCF
0.05mole of Ta in B site	Co and Fe	$Ba_{0.5}Sr_{0.5}Co_{0.76}Fe_{0.19}Ta_{0.05}O_{3-\delta}$	BSCFTa 0.05
0.1mole of Ta in B site	Co and Fe	$Ba_{0.5}Sr_{0.5}Co_{0.72}Fe_{0.18}Ta_{0.1}O_{3-\delta}$	BSCFTa 0.10
0.15mole of Ta in B site	Co and Fe	$Ba_{0.5}Sr_{0.5}Co_{0.68}Fe_{0.17}Ta_{0.15}O_{3-\delta}$	BSCFTa 0.15
0.2mole of Ta in B site	Co and Fe	$Ba_{0.5}Sr_{0.5}Co_{0.64}Fe_{0.16}Ta_{0.2}O_{3-\delta}$	BSCFTa 0.20

The BSCF perovskite anode powder was synthesized by citrate-EDTA complexing method. Perovskite material with the formula $Ba_{0.5}Sr_{0.5}Co_{0.8}Fe_{0.2}O_{3-\delta}$ (BSCF) was synthesized by using $Ba(NO_3)_2$, $Sr(NO_3)_2$, $Co(NO_3)_2 \cdot 6H_2O$ and $Fe(NO_3)_3 \cdot 9H_2O$.

Firstly, 0.04 mol of EDTA was mixed with 40 ml of 1N $\text{NH}_3\text{H}_2\text{O}$ solution to prepare a NH_3 -EDTA solution. Then, 0.01 mol of $\text{Ba}(\text{NO}_3)_2$, 0.01 mol of $\text{Sr}(\text{NO}_3)_2$, 0.016 mol of $\text{Co}(\text{NO}_3)_2 \cdot 6\text{H}_2\text{O}$ and 0.004 mol of $\text{Fe}(\text{NO}_3)_3 \cdot 9\text{H}_2\text{O}$ were added in combined solution which was heated and stirred. After that, citric acid monohydrate was added with the amount of 0.06 mol. The mole ratios of EDTA: total metal ions: citric acid monohydrate were 1: 1: 1.5. The pH of the mixture was adjusted to 6 by 25vol% ammonia solution. After continuously stirred for 1 day and heated at 120°C , the sticky gel was formed. For heat treatment, the gelled BSCF precursors were drying in oven at 110°C for 1 day. Finally, the samples were calcined at 950°C for 4 h. to obtain the BSCF powder.

The BSCFTa powders with various ratio were synthesized by the same method by using $\text{Ba}(\text{NO}_3)_2$, $\text{Sr}(\text{NO}_3)_2$, $\text{Co}(\text{NO}_3)_2 \cdot 6\text{H}_2\text{O}$, $\text{Fe}(\text{NO}_3)_3 \cdot 9\text{H}_2\text{O}$ and Ta_2O_5 . Firstly, EDTA and Ta_2O_5 were dissolved into $\text{NH}_3\text{H}_2\text{O}$ and HNO_3 , respectively. Then, the desired molar ratio of metal nitrate and 0.06 mol of citric acid monohydrate were added into the combined solution which was heated and stirred. The mole ratios of EDTA: total metal ions: citric acid monohydrate were 1: 1: 1.5. The pH of the mixture was adjusted to 6 by 25vol% ammonia solution. After continuously stirred for 1 day and heated at 120°C , the sticky gel was formed. For heat treatment, the gelled BSCFTa precursors were drying in oven at 110°C for 1 day. Finally, the samples were calcined at 950°C for 4 h. to obtain the BSCFTa powder. The condition of calcination for both BSCF and BSCFTa powders are shown in Fig. 3.2.

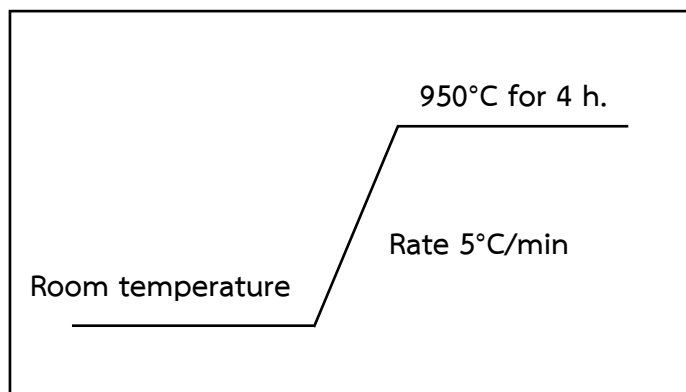


Figure 3.2 The conditions of calcination for BSCF and BSCFTa perovskite anode

The performance of different anodes including LSM-YSZ, BSCF and BSCFTa were investigated. The BSCF and BSCFTa powder were dispersed in alpha terpineol in order to obtain the anode ink. For basic anode (LSM-YSZ), the ratio between commercial powder of LSM and YSZ is 50wt%. The LSM-YSZ was dispersed in the same prepared binder. The weight ratio of these various anode powder to alpha terpineol is 1:1.

3.5 Solid oxide electrolysis cell fabrication

3.5.1 Symmetrical half-cells fabrication

The anode half cells with the configuration of BSCF/YSZ/BSCF and BSCFTa/YSZ/BSCFTa were used in this investigation. 3 g of 8% YSZ was pressed into pellets for 30s, then sintered at 1,450°C for 4 h. The BSCF or BSCFTa ink was painted onto two sides of YSZ electrolyte with the circular area of 0.19 cm², followed by sintered at 1,000°C for 2 h. The electrical connection was made on the both electrodes of the SOEC via platinum wires and paste. Finally, the cell was placed in the reactor.

3.5.2 Single cell fabrication

The full SOECs with the configuration of Ni-YSZ/YSZ/BSCF, Ni-YSZ/YSZ/BSCFTa and Ni-YSZ/YSZ/LSM-YSZ were used in this investigation. A button-type cathode-support from 3.2 was deposited by electrolyte slurry one side of the cathode by dip coating technique. Then, sintered at 1,450°C for 4 h. After that, the

BSCF, BSCFTa or LSM-YSZ ink was painted onto YSZ electrolyte with the circular area of 0.19 cm^2 , followed by sintered at $1,000^\circ\text{C}$ for 2 h. The electrical connection was made on both electrodes of the SOEC via platinum wires and paste. Finally, the cell was placed in the reactor and sealed with the glass sealant (Ultra-Temp 552, Aramco, USA).

3.6 Characterization of anode perovskite

3.6.1 X-ray diffraction (XRD)

The crystal structure of perovskite oxides was determined using Bruker D8 Advance powder X-ray diffractometer with a Cu-target X-ray tube (40kV, 30mA) and angles of 2θ range from 20-90 degree (scan step 0.02°). Perovskite were characterized after the calcination step by XRD.

3.6.2 X-ray photoelectron spectroscopy (XPS)

The valence state of O, Co and Fe of fine powder were investigated by XPS AMICUS. This instrument measures the energy of the emitting of photoelectron from the surface sample to identify the chemical valence state, binding energy and intensity of the photoelectron peak.

3.6.3 Brunauer-Emmett-Teller (BET)

The specific surface area of synthesized powders were characterized by Micromeritics ASAP2020. The BET theory is the adsorption of gas molecules on the solid surface. The amount of adsorbed gas is related to the total surface area of particle. In this experiment, the synthesized powder were characterized after the calcination step.

3.6.4 Scanning electron microscope (SEM)

The morphology of fine powder and SOECs were carried out by JEOL model S-3400. This instrument uses X-rays or electrons scattered back from the surface illuminated by a restored electron beam to generate an image with remarkable three-dimensional qualities.

3.6.5 Thermogravimetric analysis (TGA)

Thermogravimetric analysis (TGA, model SDT Q600) was performed on powder specimens from room temperature to 1,000°C using a heating rate of 20°C/min. In this experiment, the perovskite oxides were grounded into fine powder and were performed under air and N₂ atmosphere.

3.6.6 Electrochemical performance measurements

For symmetrical half-cells, electrochemical performance measurements can be studied at zero current. Electrochemical impedance spectroscopy measurement (EIS) were performed at $i_{ac}=0$ on half-cells by using a sinusoidal signal amplitude of 20mV_{rms} over the frequency range from 0.1MHz to 0.1Hz and temperature range from 650 to 800°C under air. The EIS data were collected using a potentiostat/ galvanostat (PG310 Metrohm Autolab, Netherlands), fitted with an equivalent circuit composed of a resistor in series with a parallel constant phase element (R//CPE) combinations. And The area specific resistance (ASR) was obtained from the EIS measured on the half cell. The activation energy of the BSCFTa with different Ta⁵⁺ content was calculated from the Arrhenius plot between the ASR and a range operating temperature as shown in Eq. (3.1)

$$ASR = A \cdot e^{-E_a/K_B T} \quad (3.1)$$

where ASR is area specific resistance ($\Omega \cdot \text{cm}^2$); A is pre-exponential factor; T is the absolute temperature (K); E_a is the activation energy of oxygen electrode (eV) and K_B is the Boltzmann's constant ($8.61 \times 10^{-5} \text{ eV} \cdot \text{K}^{-1}$).

For single cell measurements, I/V curve were measured by using linear sweep current techniques. A potentiostat/ galvanostat operating in galvanostatic mode was used to control the voltage between 0.6 and 1.8V, using scan rate of 0.1V/s. The test system allowed gas composition of H₂/N₂ to be introduced into cathode chamber using varied steam to hydrogen ratio (60:40, 70:30 and 90:10) under the operating temperature was controlled between 650 to 900°C. And EIS measurements were

performed across the frequency range of 0.1MHz to 0.1Hz with an equivalent circuit composed of a resistor in series with two parallel constant phase element (R//CPE) combinations. The operating condition and experimental set up were shown in Table 3.5 and Fig. 3.3, respectively.

Table 3.5 Steam to H₂ ratio of operating condition

Steam to H ₂ ratio	H ₂ flow (ml/min)	N ₂ flow (ml/min)	Steam flow (ml/min)	Water pump (μl/min)	Total gas flow to cathode (ml/min)
60: 40	100	75	150	121	325
70: 30	75	75	175	141	325
90: 10	25	75	225	181	325

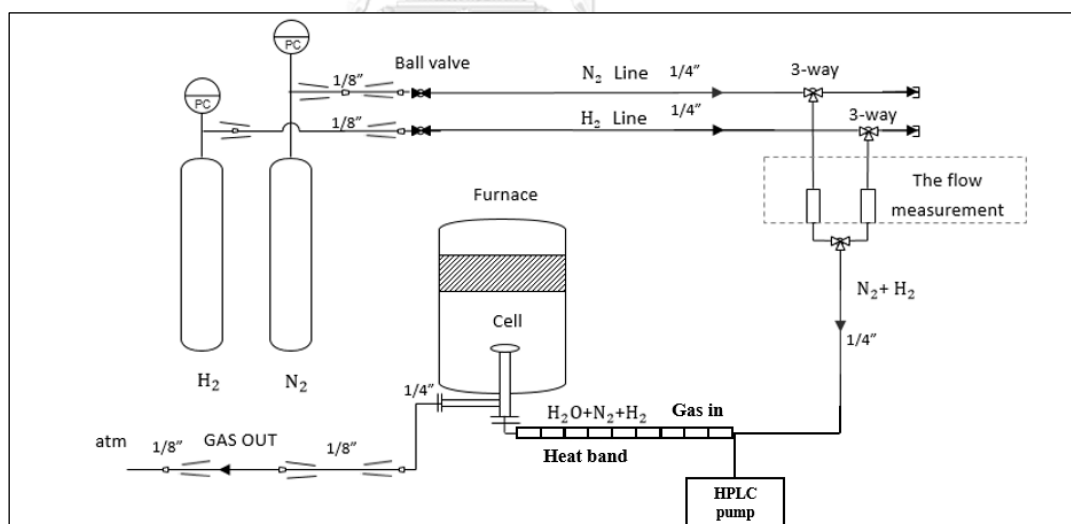


Figure 3.3 Schematic drawing of the test system

CHAPTER IV

RESULTS AND DISCUSSION

4.1 Structural characterization

X-ray diffraction (XRD) patterns of the synthesized $\text{Ba}_{0.5}\text{Sr}_{0.5}(\text{Co}_{0.8}\text{Fe}_{0.2})_{1-x}\text{Ta}_x\text{O}_{3-\delta}$ where x is 0, 0.05, 0.1, 0.15 and 0.2 were shown in Fig. 4.1. For BSCFTa0.05, the main peaks presented a single phase with cubic perovskite structure (Pm3m), corresponding to peaks at (100), (110), (111), (200), (210), (211), (220) and (310) (JCPDS No. 01-079-5253). As shown in the magnified scaled in Fig.4.1(b), increasing Ta^{5+} -doping introduced a shift in the peak positions (110) to a higher diffraction angle due to a lower lattice parameter. The lattice parameter were 3.9872, 3.9856, 3.9825, 3.9777 and 3.9699 Å, while the lattice volume were 63.3875, 63.3112, 63.1636, 62.9355 and 62.5660 Å³ for BSCF, BSCFTa0.05, BSCFTa0.10, BSCFTa0.15 and BSCFTa0.20, respectively. It should be noted that the ionic radius of Ta^{5+} (0.064nm) is relative smaller than the host (0.074nm for Co^{2+} and 0.064nm for Fe^{3+}). The peak shifting to a higher diffraction angle implied that the hosts were Co^{2+} and Fe^{3+} rather than Co^{4+} (0.053nm) and Fe^{4+} (0.058nm) which are smaller than Ta^{5+} . The formation of Co^{2+} and Fe^{3+} was resulted by the substitution of higher valence Ta^{5+} on the B-site which required the compensation of positive charges by decreasing the valence state of cobalt and iron cations (electronic compensation). In addition, the charge balance can be maintained by ionic compensation by decreasing the oxygen vacancy concentration [29]. Furthermore, the lower of lattice parameter and unit cell volume could be consistent with the Ta^{5+} -doping at B-site on BSCF. The more Ta^{5+} -doping at B-site, the more of segregation phase of Ta_2O_5 and Ta_3N_5 , as shown in Fig. 4.1(b). The XRD pattern that a dominant peak of Ta_3N_5 (JCPDS No. 79-1533) observed at 31.3 of 2θ and peaks of Ta_2O_5 (JCPDS No. 29-1149) were also clearly observed in BSCFTa0.20. The shift in XRD peaks indicated that Ta^{5+} incorporated in the BSCF structure forming a solid solution. Furthermore, sharp and high intensity XRD peaks were observed from BSCF without Ta^{5+} -dopant, indicating the higher crystallinity and

the larger crystallite size. The average crystallite size of BSCF, BSCFTa0.05, BSCFTa0.10, BSCFTa0.15, BSCFTa0.20 were 46.3, 45.0, 33.9, 28.4, and 38.0 nm, respectively. The crystallite size tended to decrease with increasing Ta⁵⁺ content. The change of crystal nanostructure was probably because doping of highly charge ferroactive cation, Ta⁵⁺, on the B-site could suppress the perovskite phase transition from cubic to hexagonal [30].

The SEM images and the EDX mapping of BSCFTa perovskite powder after calcination at 950°C for 4h were shown in Fig. 4.2 and Fig. 4.3, respectively. The BSCF was clearly seen as agglomerated and large particles. Conversely, the particle size of the BSCFTa were relatively smaller than the BSCF, corresponding to the XRD patterns which show broader main-peaks. As can be seen in Fig. 4.3, EDX element mapping showed a homogeneous distribution of Ba, Sr, Co, Fe and Ta in the samples. Ta content was more pronounced in BSCFTa0.20 due to the formation of Ta-rich phases of Ta₂O₅ and Ta₃N₅. Furthermore, the element composition on surface of each anode was shown in Table. 4.1. And the specific surface area were 5.58, 5.79, 3.86, 3.55 and 2.94m²/g for BSCF, BSCFTa0.05, BSCFTa0.10, BSCFTa0.15 and BSCFTa0.20, respectively. The decrease of specific surface area with increasing of Ta⁵⁺ content may relate to the formation of Ta₂O₅ and Ta₃N₅ phases.

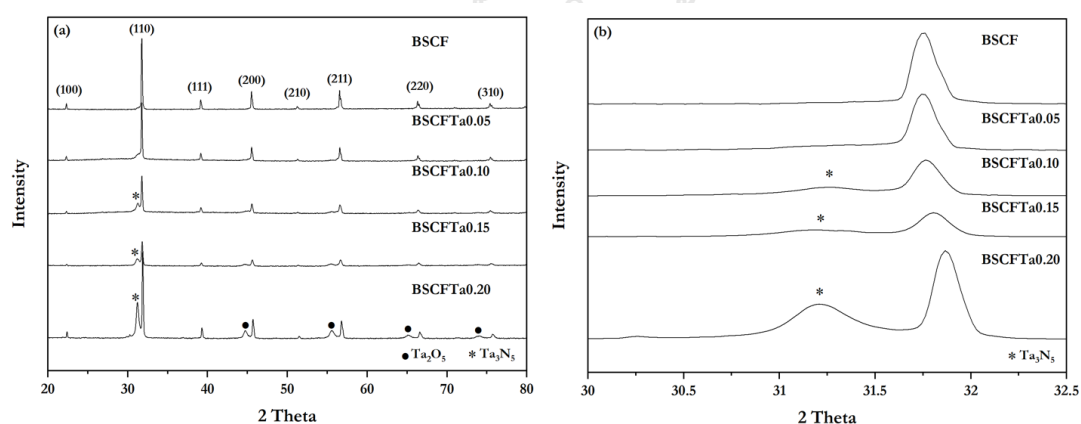


Figure 4.1 XRD patterns of $\text{Ba}_{0.5}\text{Sr}_{0.5}(\text{Co}_{0.8}\text{Fe}_{0.2})_{1-x}\text{Ta}_x\text{O}_{3-\delta}$ (BSCFTa) where $x = 0, 0.05, 0.1, 0.15$ and 0.2 : **(a)** after calcined at 950°C for 4h; and **(b)** magnified scale at 2 Theta angles between 30° and 32.5°

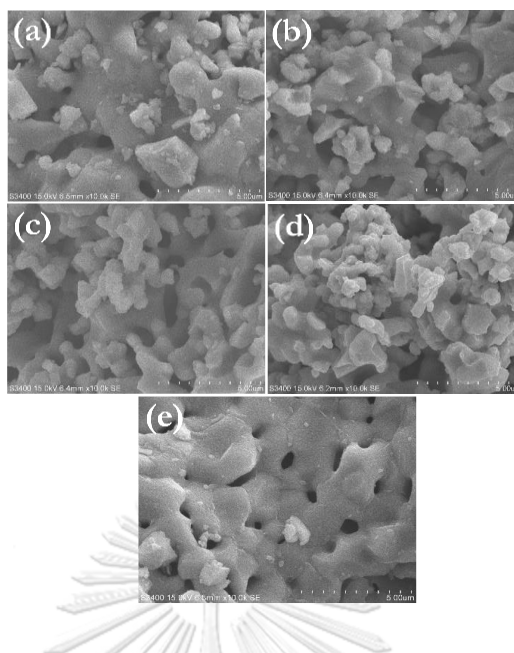


Figure 4.2 SEM images of $\text{Ba}_{0.5}\text{Sr}_{0.5}(\text{Co}_{0.8}\text{Fe}_{0.2})_{1-x}\text{Ta}_x\text{O}_{3-\delta}$ (BSCFTa) calcined at 950°C for 4h: (a) BSCFTa0.05, (b) BSCFTa0.10, (c) BSCFTa0.15, (d) BSCFTa0.20 and (e) BSCF

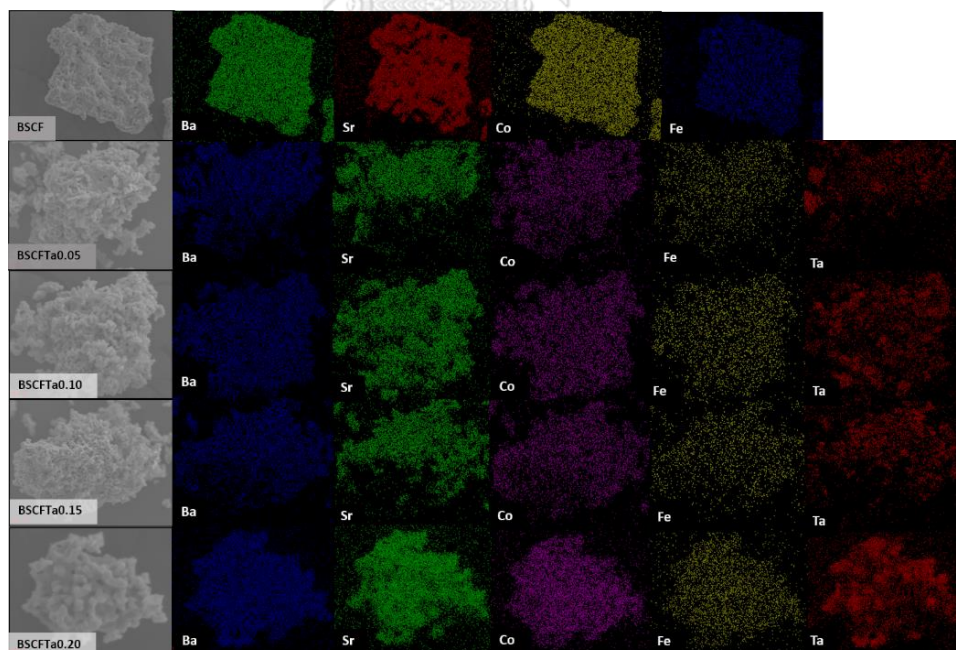


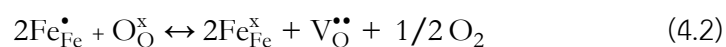
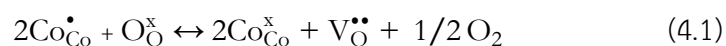
Figure 4.3 EDX images of $\text{Ba}_{0.5}\text{Sr}_{0.5}(\text{Co}_{0.8}\text{Fe}_{0.2})_{1-x}\text{Ta}_x\text{O}_{3-\delta}$ (BSCFTa) fine powder where $x = 0, 0.05, 0.1, 0.15$ and 0.2 which calcined at 950°C for 4h.

Table 4.1 The stoichiometry of $\text{Ba}_{0.5}\text{Sr}_{0.5}(\text{Co}_{0.8}\text{Fe}_{0.2})_{1-x}\text{Ta}_x\text{O}_{3-\delta}$ ($0 \leq x \leq 0.2$) anode calculated from EDX analysis.

Anode	EDX results				
	Ba	Sr	Co	Fe	Ta
$\text{Ba}_{0.5}\text{Sr}_{0.5}\text{Co}_{0.8}\text{Fe}_{0.2}\text{O}_{3-\delta}$	0.53	0.46	0.83	0.18	0
$\text{Ba}_{0.5}\text{Sr}_{0.5}\text{Co}_{0.76}\text{Fe}_{0.19}\text{Ta}_{0.05}\text{O}_{3-\delta}$	0.53	0.50	0.70	0.20	0.07
$\text{Ba}_{0.5}\text{Sr}_{0.5}\text{Co}_{0.72}\text{Fe}_{0.18}\text{Ta}_{0.1}\text{O}_{3-\delta}$	0.54	0.40	0.76	0.18	0.12
$\text{Ba}_{0.5}\text{Sr}_{0.5}\text{Co}_{0.68}\text{Fe}_{0.17}\text{Ta}_{0.15}\text{O}_{3-\delta}$	0.51	0.53	0.70	0.16	0.17
$\text{Ba}_{0.5}\text{Sr}_{0.5}\text{Co}_{0.64}\text{Fe}_{0.16}\text{Ta}_{0.2}\text{O}_{3-\delta}$	0.52	0.42	0.72	0.16	0.20

4.2 Thermogravimetric analysis

The thermal behaviour of BSCFTa ($0 \leq x \leq 0.2$) were measured using TGA, as shown in Fig.4.4 The weight loss of samples were measured in air and N_2 atmosphere between room temperature and 800°C . In the TGA profiles under air atmosphere, the weight loss was related to the oxidation and the thermal reduction of metal ions. At the first state, the weight reduced from room temperature to 200°C , which was ascribed to the water desorption [20]. At the second state, the change of weight loss of all samples slowed down around 200°C to 400°C due to the oxidation of Co^{2+} and Fe^{3+} at the B-site to their higher valence (Co^{4+} and Fe^{4+}), resulting in oxygen gain [20]. At the third state, the weight obviously decreased at the temperature from 400°C to 800°C , which was related to thermal reduction of Co^{4+} and Fe^{4+} to their lower valence state (Co^{3+} and Fe^{3+}), leading to a larger ionic radius and a loss of lattice oxygen, in turns increasing the oxygen vacancies [31, 32]. This reaction associated with the Kroger-Vink notation, as expressed in Eq. (4.1) and Eq. (4.2), respectively:



where $\text{Co}_{\text{Co}}^{\bullet}$, $\text{Co}_{\text{Co}}^{\times}$; $\text{Fe}_{\text{Fe}}^{\bullet}$ and $\text{Fe}_{\text{Fe}}^{\times}$ represent the change of valence state of Co and Fe cations from 4+ to 3+. When weight loss increased with increasing the temperature, the equation will shift to the right and induced the formation of oxygen vacancies. The weight loss of all samples that measured in air was less than that in N_2 atmosphere. Operating the BSCFTa electrode under low oxygen partial pressure increased oxygen vacancies inside the lattice structure and can lead to a larger weight loss in N_2 atmosphere [33, 34]. However, more oxygen vacancies concentration can increase oxygen transportation. As shown in Fig. 4.4, the weight loss in air for BSCF, BSCFTa0.05, BSCFTa0.10, BSCFTa0.15 and BSCFTa0.20 were 1.41%, 1.57%, 1.36%, 1.47% and 1.32%, respectively. The weight loss in N_2 atmosphere were 1.99%, 2.09%, 1.92%, 2.04% and 1.89%, respectively. The weight loss of Ta-doped samples tended to be smaller than that of BSCF in both of atmosphere, which represented a smaller oxygen vacancies in the BSCF perovskite structure and diminished the oxygen release from the lattice structure [34, 35].

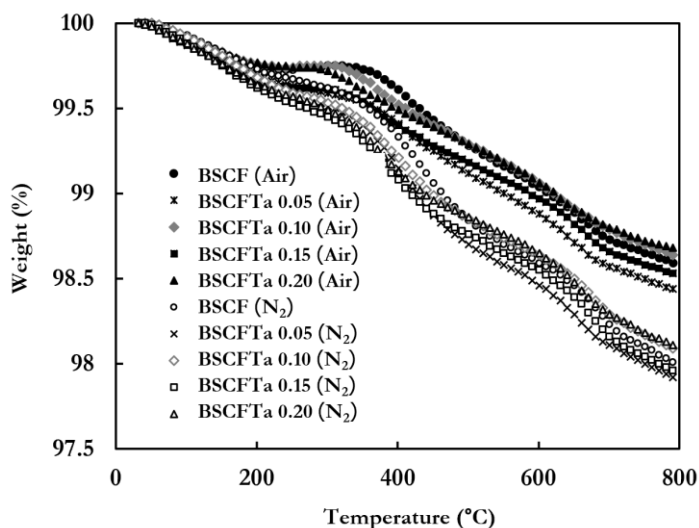
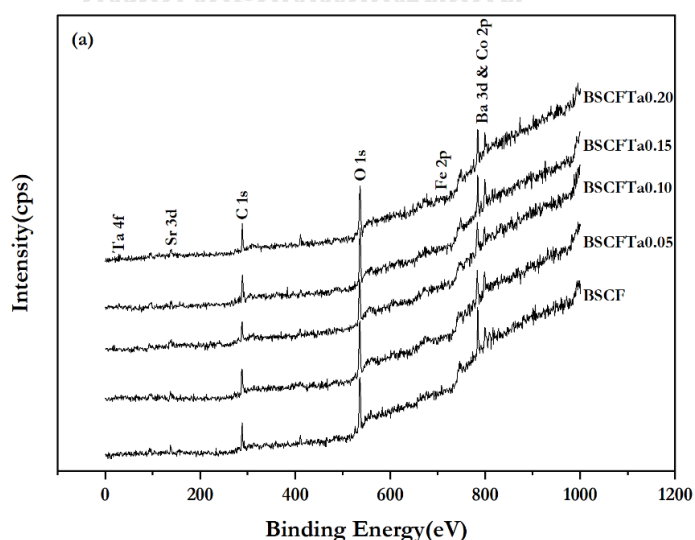


Figure 4.4 TGA profile of $\text{Ba}_{0.5}\text{Sr}_{0.5}(\text{Co}_{0.8}\text{Fe}_{0.2})_{1-x}\text{Ta}_x\text{O}_{3-\delta}$ (BSCFTa), where $x=0, 0.05, 0.1, 0.15$ and 0.2 , in air and N_2 at temperature ranging from room temperature to 800°C

4.3 X-ray photoelectron spectroscopy analysis

The valence state of O1s, Co2p and Fe2p on BSCFTa ($0 \leq x \leq 0.2$) perovskite were characterized by XPS. As shown in Fig. 4.5(a), the Ba3d, Sr3d, Co2p, Fe2p, Ta4f, O1s and C1s were observed on the XPS survey spectra. The O1s signal was deconvoluted into three peaks, as shown in Fig. 4.5(b). The peaks around 529eV and 532eV can be assigned to the lattice oxygen species (O_{lattice}), which were related to the metal ions at A and B site and the peaks around 533eV can be ascribed to the adsorbed oxygen vacancies (O_{adsorbed}) [36-38]. Normally, the ratio of O_{adsorbed} and O_{lattice} is associated with the oxygen vacancies on the perovskite lattice, which can be calculated from the area under the XPS peaks [39]. As shown in Table. 4.2, the $O_{\text{adsorbed}}/O_{\text{lattice}}$ decreased slightly as increasing a partial Ta^{5+} substitution on B-site to BSCFTa0.05 and BSCFTa0.10. Then the formation of oxygen vacancy decreased abruptly when further increased the Ta^{5+} to BSCFTa0.15 and BSCFTa0.20. The decrease of $O_{\text{adsorbed}}/O_{\text{lattice}}$ at high ratio of Ta^{5+} doping could be attributed to the compensation of positive charges by decreasing of oxygen vacancy concentration. This indicated that the oxygen vacancies in the BSCF lattice structure decreased with Ta^{5+} -doping, desirable for the stability of BSCF anode. This results was corresponded well with high-charged doping BSCF such as W^{6+} [40].



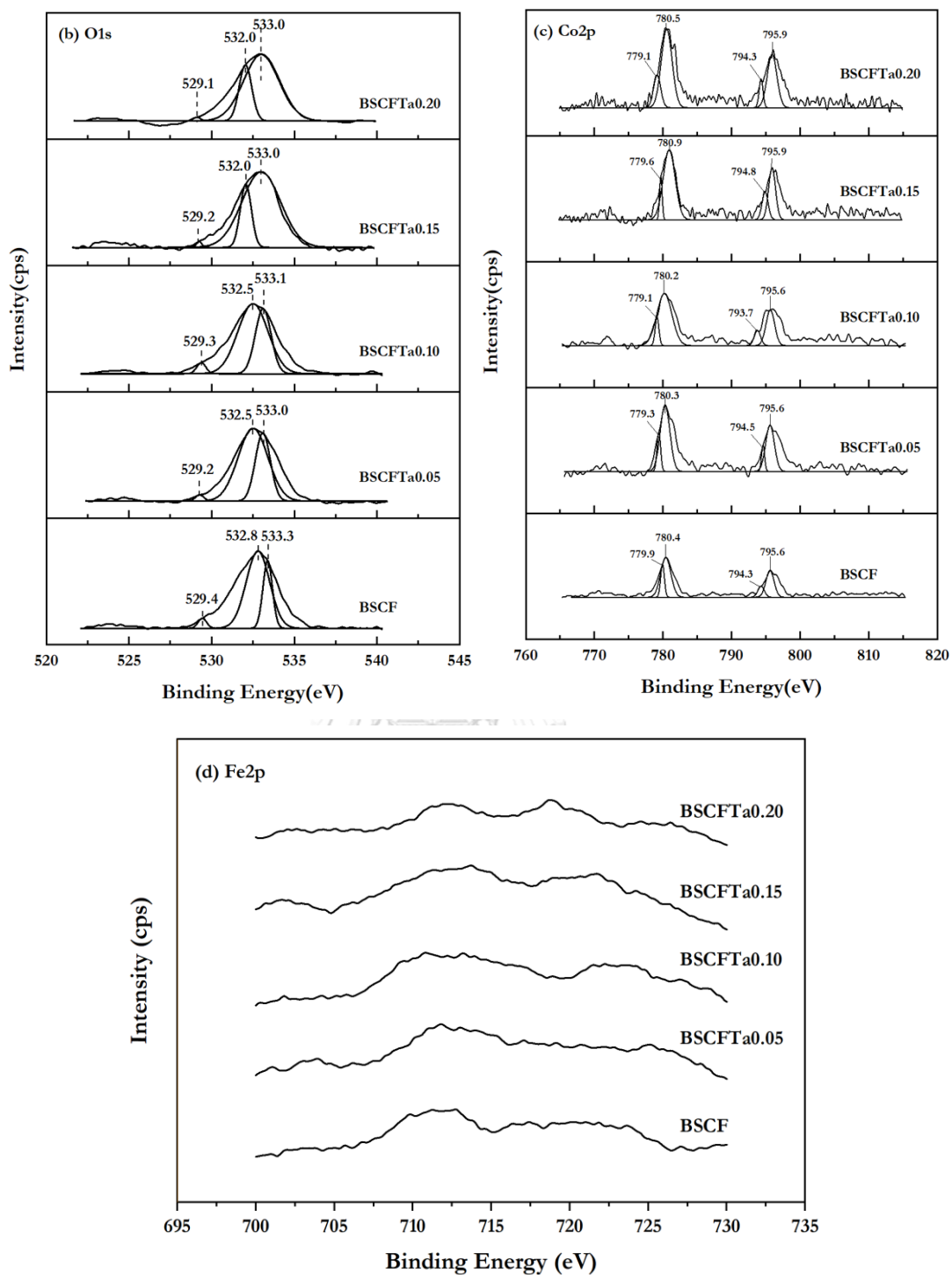


Figure 4.5 The XPS spectra of $\text{Ba}_{0.5}\text{Sr}_{0.5}(\text{Co}_{0.8}\text{Fe}_{0.2})_{1-x}\text{Ta}_x\text{O}_{3-\delta}$ ($0 \leq x \leq 0.2$) powder: **(a)** Low resolution XPS scan, **(b)** O1s XPS spectra, **(c)** Co2p XPS spectra and **(d)** Fe2p XPS spectra

Table 4.2 The area of the XPS peaks representing different kinds of oxygen species and the ratio of $O_{\text{adsorbed}}/O_{\text{lattice}}$ in $Ba_{0.5}Sr_{0.5}(Co_{0.8}Fe_{0.2})_{1-x}Ta_xO_{3-\delta}$ ($0 \leq x \leq 0.2$)

x value in $Ba_{0.5}Sr_{0.5}(Co_{0.8}Fe_{0.2})_{1-x}Ta_xO_{3-\delta}$	%Area		$O_{\text{adsorbed}}/O_{\text{lattice}}$
	O_{adsorbed}	O_{lattice}	
0	71.44	28.56	2.50
0.05	66.91	33.09	2.02
0.10	65.16	34.84	1.87
0.15	19.25	80.75	0.24
0.20	22.55	77.45	0.29

For deconvolution of the Co2p XPS spectra, four peaks and two signals of Co orbit were obtained, as shown in Fig. 4.5(c). The peaks at 779eV and 780eV in Co2p_{3/2} can be assigned to Co³⁺ and Co⁴⁺, respectively. The peaks at 794eV and 795eV in Co2p_{1/2} can be ascribed to Co³⁺ and Co⁴⁺, respectively. The higher peak in Co2p_{3/2} (780eV) and Co2p_{1/2} (795eV) typically attributed to Co⁴⁺ due to the electron density of Co⁴⁺ is higher than Co³⁺, which were located at higher binding energy [35, 37, 38]. The lower valence Co²⁺ can be indicated in the range between 785eV and 788eV of binding energy. However, it was observed that there were nearly no satellite peaks when compared the peak intensities to Co³⁺ and Co⁴⁺ peaks [38, 41]. Hence, the concentration of Co²⁺ can be neglected. As shown in Table 4.3, the Co³⁺/Co⁴⁺ decreased with increasing the Ta⁵⁺-doping at B-site to BSCFTa0.05 and BSCFTa0.10. Then the Co³⁺/Co⁴⁺ tended to increase as increasing the Ta⁵⁺ dopant on BSCFTa0.15 and BSCFTa0.20. The lowest of Co³⁺/Co⁴⁺ on BSCFTa0.10, showed a beneficial on the structural stability of BSCFTa0.10 anode due to a slightly reduction of Co⁴⁺ into Co³⁺. Moreover, the more of Co⁴⁺ content can be resulted to the higher of electrical conductivity and indicated to the higher of charge transfer [31]. In addition, it should be noted that the higher valence state of Co ions was reported to increase the acidity of BSCF and the higher acidity leads to better resistance against CO₂ in air - reducing carbonate formation [42, 43].

Table 4.3 The area of the XPS peaks representing different kinds of Co ions and the ratio of $\text{Co}^{3+}/\text{Co}^{4+}$ in $\text{Ba}_{0.5}\text{Sr}_{0.5}(\text{Co}_{0.8}\text{Fe}_{0.2})_{1-x}\text{Ta}_x\text{O}_{3.6}$ ($0 \leq x \leq 0.2$)

x value in $\text{Ba}_{0.5}\text{Sr}_{0.5}(\text{Co}_{0.8}\text{Fe}_{0.2})_{1-x}\text{Ta}_x\text{O}_{3.6}$	%Area		$\text{Co}^{3+}/\text{Co}^{4+}$
	Co^{3+}	Co^{4+}	
0	23.73	76.27	0.31
0.05	17.64	82.36	0.21
0.10	15.76	84.24	0.18
0.15	19.09	80.91	0.23
0.20	20.36	79.64	0.25

As shown in Fig. 4.5(a), both intensities and area under XPS spectra of Fe2p were nearly invisible. However, the Fe2p XPS region can be indicated into two components (Fe^{3+} and Fe^{4+}). As presented in Fig. 4.5(d), the peaks around 710eV and 712eV in $\text{Fe}2p_{3/2}$ can be ascribed to Fe^{3+} and Fe^{4+} , respectively. The peak at 723eV and 725eV in $\text{Fe}2p_{1/2}$ can be attributed to Fe^{3+} and Fe^{4+} , respectively. Moreover, the satellite peaks appearing at around 719eV was also presented of Fe^{3+} [35, 36, 44]. It is rather difficult to quantify the area under Fe2p XPS spectra, due to the small concentration of Fe in $\text{Ba}_{0.5}\text{Sr}_{0.5}(\text{Co}_{0.8}\text{Fe}_{0.2})_{1-x}\text{Ta}_x\text{O}_{3.6}$.

4.4 Calculation of tolerance factor (t)

In BSCF perovskite structure, Ba and Sr ions exhibit a fixed valence state of +2 while Co and Fe ions in B-site can have multi-valence states and their contents vary with oxygen partial pressure and temperature. From the XPS analysis, Co ions were Co^{3+} and Co^{4+} , as shown in Table. 4.2. And the valence state of Fe takes the Fe^{3+} and Fe^{4+} . It should be noted that Fe^{2+} can occur at the temperature above 1150°C [45]. Hence, for the temperature ranges between 600°C and 800°C in this study, two possible conditions of the Co and Fe valence states are assumed: t' (Co^{3+} , Co^{4+} , Fe^{3+}) and t'' (Co^{3+} , Co^{4+} , Fe^{4+}), respectively. The tolerance factor of these two conditions was calculated from Eq. (2.4). As presented in Fig. 4.6, the tolerance factor decreased with increasing Ta^{5+} content in both t' and t'' conditions. The fixed

valence state of Ta^{5+} can stabilize the charged cation on B-site due to the attracting electron density of Co ion by the excess positive charge of Ta^{5+} [46]. Moreover, doping with different amounts of Ta^{5+} at B-site in BSCF resulted in the lower oxygen vacancy formation, increasing the stability of the cubic BSCF structure and the tolerance factor is nearly to 1 of all valence state (t' and t'').

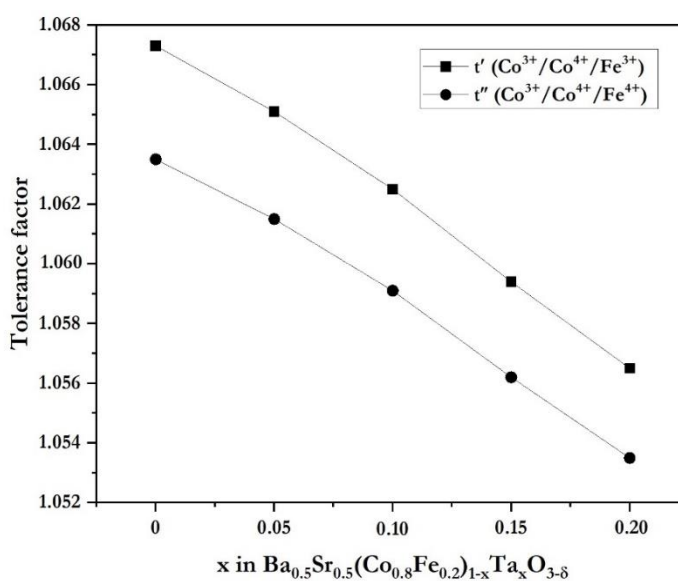


Figure 4.6 Tolerance factor of $Ba_{0.5}Sr_{0.5}(Co_{0.8}Fe_{0.2})_{1-x}Ta_xO_{3-\delta}$ (BSCFTa), where $x = 0, 0.05, 0.1, 0.15$ and 0.2 with various valence state of Co and Fe metal ions at room temperature.

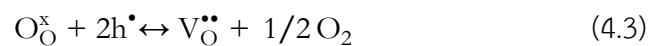
CHULALONGKORN UNIVERSITY

4.5 Electrochemical performance

4.5.1 Electrochemical performance of symmetrical half-cell

The EIS measurement was studied under ambient air by using symmetrical half-cell with YSZ as an electrolyte (BSCFTa/ YSZ/ BSCFTa). In general, the interpretation of anodic polarization for symmetrical half-cell can be expressed into two partially resolved arcs: the arc at high frequency (HF) and low frequency (LF). The HF-intercept represents the ohmic resistance (R_{Ohmic}) of the cell, which was associated with the electrolyte lattice resistance and lead response. Charge transfer was

represented by the HF arc (R_{HF}) while the mass transport which was related to the gas phase diffusion was represented by the LF arc (R_{LF}) [23, 47]. In this study, the EIS diagrams were fitted into an equivalent circuit which was a combination of a resistor in series with a parallel constant phase element (CPE)/resistor combination. As can be seen in Fig. 4.7(a) and inset, the summative result of single arc from Nyquist plot and R_{CT} parameter is charge transfer resistance. In this study, the frequency of single arc of each symmetrical half-cell were in the range of 50.11-316.23Hz which corresponding to the oxide transfer in electrode [48]. And the capacitance value was 10^{-4} F which can be associated with the electrochemical reaction [49, 50]. The ohmic resistance of symmetrical half-cell having various Ta^{5+} contents were in the range of 7.50-8.37 $\Omega \cdot cm^2$. For single arc in EIS plot, it can be associated with the charge transfer at electrode and electrolyte interface including the transport of oxygen ion (O^{2-}) and O^{2-} to O_2 on oxidation reaction while the gas diffusion process was negligible [51, 52]. Furthermore, the interpretation of charge transfer resistance can be responded to the total polarization resistance in case of single arc. The trend of total polarization resistance decreased with a partial substituting of Ta^{5+} at B-site in BSCF. Moreover it was found the total polarization resistance of BSCFTa0.10 was the lowest, which can be explained by the properties of mixed ionic and electronic conductivity (MIEC) on BSCFTa material and the properties of highly charge (Ta^{5+}) dopant at B-site on BSCF and. The balance in MIEC, which presence of oxygen vacancies and electronic holes is the key on oxygen electrode performance. As presented in Eq. (4.3).

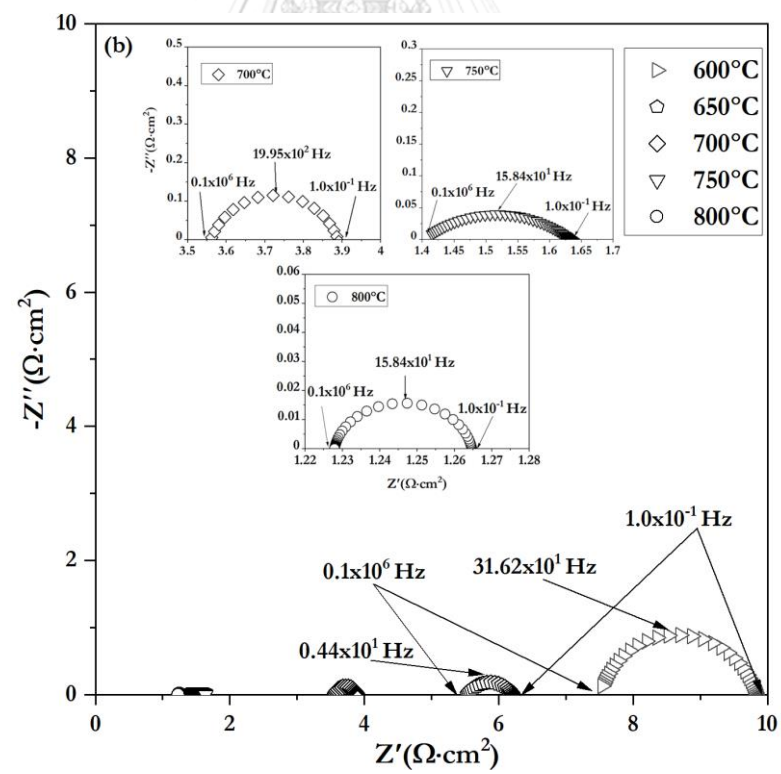
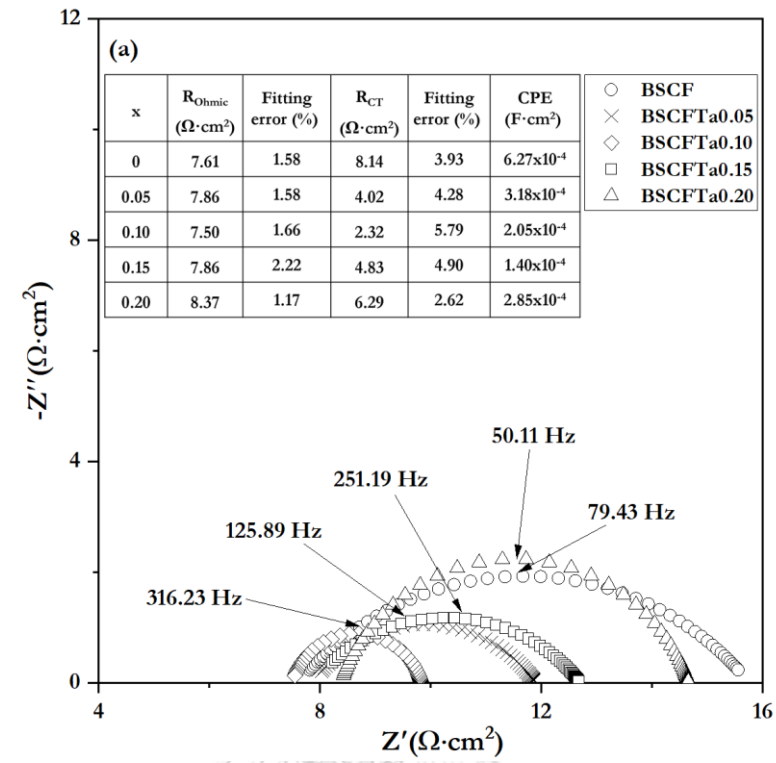


where $2h^\bullet$ is the electron hole, O_O^x is lattice oxygen and $V_O^{\bullet\bullet}$ is oxygen vacancy. The more oxygen vacancy, the smaller of electron holes [24, 31, 40]. As the result from XPS, comparing the BSCFTa0.10 with BSCFTa0.15 and BSCFTa0.20, BSCFTa0.10 shown the higher oxygen vacancy, which resulting in the greater oxygen mobility during the oxygen diffusion process on oxygen electrode. Whereas BSCFTa0.10 shown a slightly lower of oxygen vacancy when compared with the BSCFTa0.05 and BSCF but

BSCFTa0.10 led to the higher on electronic hole. Furthermore, the chemical properties of Ta⁵⁺ that contain the lower electronegativity can be induced a slightly of Co valence and resulting in the more concentration of oxygen vacancy [46, 53]. Hence, neither more nor less on oxygen vacancy of BSCFTa0.10 was properly on amount of Ta⁵⁺ dopant for optimum the oxygen electrode performance and shown the lowest on total polarization resistance.

The EIS of BSCFTa0.10 under the different operating temperature between 600°C and 800°C was investigated, as shown in Fig. 4.7(b) It can be clearly seen that the temperature had an influence on the total polarization resistance. The polarization resistance decreased with increasing the temperature and the measured values were 2.32, 0.72, 0.34, 0.22 and 0.04 $\Omega\text{-cm}^2$ for 600, 650, 700, 750 and 800°C, respectively.

The area specific resistance (ASR) of symmetrical half-cells with the configuration of BSCFTa/ YSZ/ BSCFTa under the operating temperature range from 600 to 800°C in ambient air was evaluated, as presented in Fig. 4.7(c). The ASR of all samples decreased with increasing the temperature. And the trend of ASR decreased with decreasing the Ta⁵⁺ content, which related to the total polarization resistance as shown in Fig. 4.7(a). Furthermore, the activation energy (E_a) of oxygen electrode for the oxygen oxidation reaction was also calculated from the plot of ASR and the range of operating temperature. The activation energy was slightly increased with increasing the partial substituting Ta⁵⁺ at B-site on BSCF with a value of 1.53, 1.55, 1.48, 1.56 and 1.57eV for BSCF, BSCFTa0.05, BSCFTa0.10, BSCFTa0.15 and BSCFTa0.20, respectively. This result suggests BSCFTa0.10 is a promising candidate as an oxygen electrode due to the smallest on activation energy and total polarization resistance, which can be beneficial on the faster of oxygen permeability including oxygen oxidation process and O²⁻ ions transportation [54]. In addition, the value of oxygen vacancy on BSCFTa0.10 can be recommended as the appropriately value in term of balance between electron hole and oxygen vacancy which can be improved the electrochemical performance while maintaining its chemical stability as an oxygen electrode.



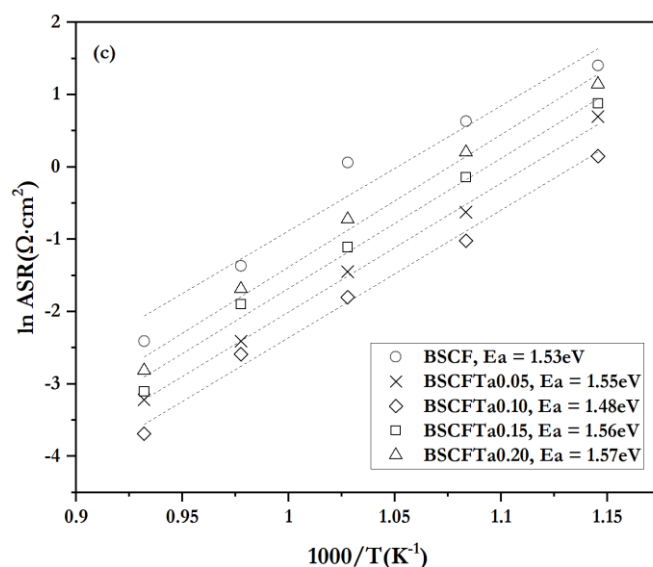


Figure 4.7 The EIS response: **(a)** impedance plot of the symmetrical half-cell with different Ta⁵⁺-doping on BSCF at 600°C, inset is the summarize results from EIS curves; **(b)** impedance plot of half-cell with configuration of BSCFTa0.10/YSZ/BSCFTa0.10 under various operating temperature in air, inset is the magnified image of EIS response at 700°C, 750°C and 800°C; and, **(c)** Arrhenius plot of temperature dependence of the ASR of the various Ta⁵⁺-doping on BSCF anode on YSZ electrolyte

4.5.2 Electrochemical performance of cathode-supported cell

The electrochemical performance of the cathode-supported SOEC was measured. The I/V response of the SOEC having BSCFTa0.10 anode was compared to undoped BSCF and LSM-YSZ a basic anode, presented in Fig. 4.8. The cell was measured between applied voltage of 0.6 and 1.8V at 800°C and steam to H₂ ratio of 70:30 was introduced at the cathode chamber, while at the anode using an ambient air. The cathode-supported Ni-YSZ/YSZ/BSCFTa0.10 exhibited the highest performance in both SOEC and SOFC mode, while Ni-YSZ/YSZ/LSM-YSZ was the lowest performance. The current density of Ni-YSZ/YSZ/BSCFTa0.10 was 8.3 times greater than Ni-YSZ/YSZ/BSCF at 1.8V, indicating that partial substituting BSCF with Ta⁵⁺ at B-site enhanced a great performance on oxygen electrode. The H₂ production rate by Faraday's law were calculated. At applied voltage at 1.1, 1.5 and 1.8V, the H₂

production rate was 0.31, 0.61 and 0.83 $\mu\text{mol}\cdot\text{s}^{-1}$, respectively for Ni-YSZ/YSZ/BSCF. The rate was 3.14, 5.29 and 6.99 $\mu\text{mol}\cdot\text{s}^{-1}$, respectively for Ni-YSZ/YSZ/BSCFTa0.10. And the rate was 0.13, 0.34 and 0.50 $\mu\text{mol}\cdot\text{s}^{-1}$, respectively for Ni-YSZ/YSZ/LSM-YSZ. The H_2 production rate of all anode increased with increasing the applied voltage.

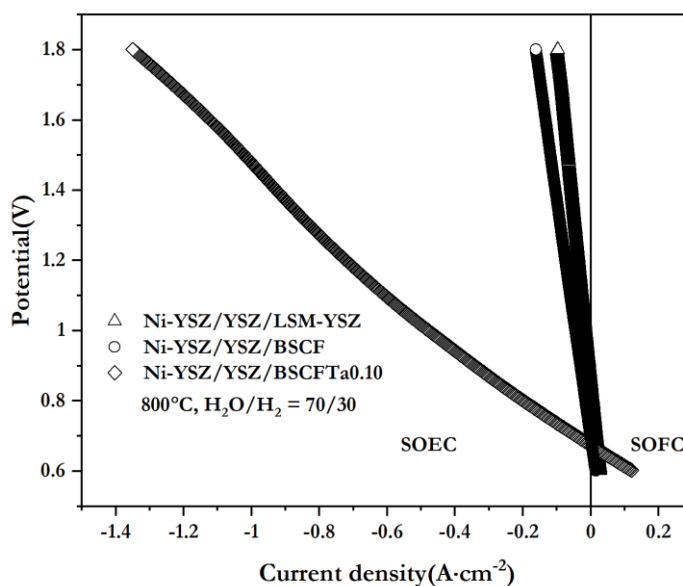


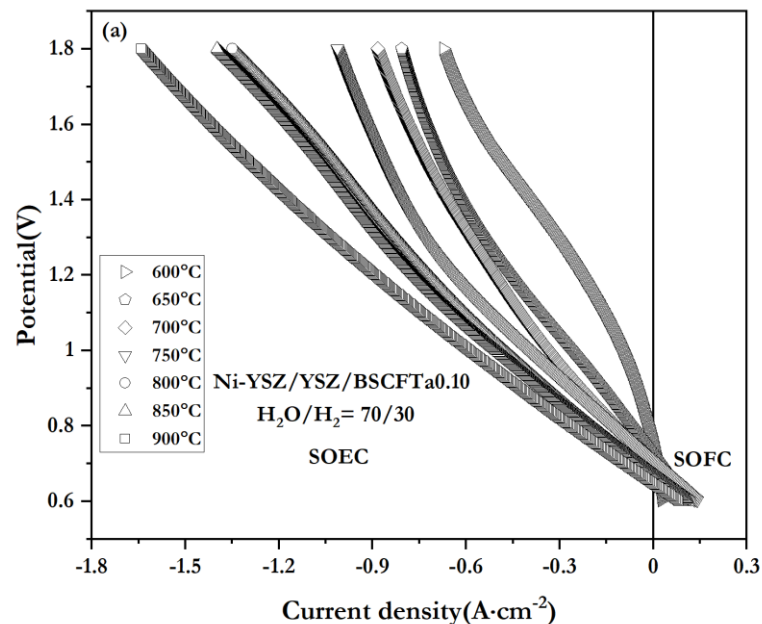
Figure 4.8 The I/V response of Ni-YSZ/YSZ/Anode when the anode was BSCF, BSCFTa0.10 and LSM-YSZ, operated at 800°C under steam to H_2 ratio of 70:30

As can be seen in Fig. 4.9(a), the effect of different operating temperature, while the steam to H_2 was controlled at constant 70:30 on SOEC performance was studied. As the temperature increased from 600°C to 900°C, the current density of cathode-supported having BSCFTa0.10 anode increased. It can be indicated that the performance on SOEC was improved with increasing the operating temperature. According to the Nernst equation, the open circuit voltage (OCV) would decrease from 0.97V to 0.86V when the temperature increased from 600°C to 900°C. However, in this study the measure OCV of Ni-YSZ/YSZ/BSCFTa0.10 was approximately 0.7V, which correspond to the leakage in sealing around the cell.

The effect of variables of steam content, while the operating temperature was maintained constant at 800°C was shown in Fig. 4.9(b). The current density of 0.93,

1.02 and 1.06 $\text{A}\cdot\text{cm}^{-2}$ were obtained at 1.5V with steam to H_2 of 60:40, 70:30 and 90:10, respectively. It can be indicated that the current density increased when increasing the proportion of steam to H_2 , which can be relate higher steam in gas feed for steam electrolysis and can be induced the higher H_2 production [55].

The EIS measurement of single cell having BSCFTa0.10 anode in electrolysis and fuel cell mode at 800°C and steam to H_2 ratio of 70:30 were investigated, as shown in Fig. 4.9(c). The EIS diagrams were fitted into an equivalent circuit which was a combination of a resistor in series with two parallel constant phase element (CPE)/resistor combinations. The total polarization resistance of electrolysis mode was 1.82 times larger than fuel cell mode, which showed lower performance in electrolysis mode. In addition, two arcs of R_{HF} and R_{LF} on SOEC mode were observed. R_{LF} represent the mass transport on gas diffusion, which can be occurred from the thickness of cathode layer. Meanwhile, R_{HF} on SOEC mode was significantly higher than R_{LF} , corresponding to the main characteristic on oxygen ion mobility as same as the BSCFTa on symmetrical half-cell.



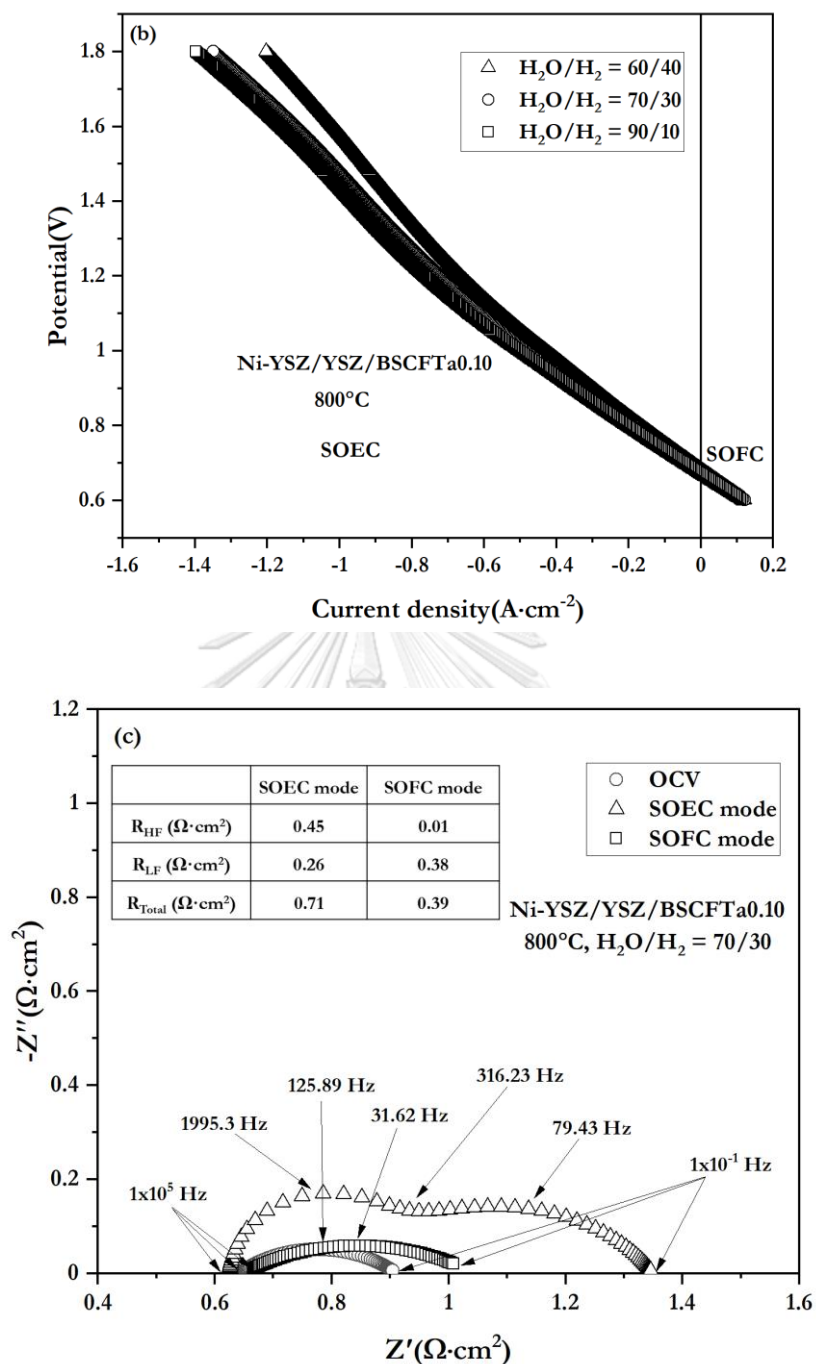


Figure 4.9 The I/V response of Ni-YSZ/YSZ/BSCFTa0.10: **(a)** Effect of operating temperature (steam to H_2 ratio of 70:30); **(b)** Effect of steam to H_2 ratio operating temperature at 800°C; and **(c)** The EIS response of Ni-YSZ/YSZ/BSCFTa0.10 in electrolysis (1.1v) and fuel cell mode (0.6v) under steam to H_2 ratio of 70:30 at 800°C, inset is the summarize results from fitted EIS curves

4.5.3 Durability test

The durability test of Ni-YSZ/YSZ/BSCFTa0.10 comparing with Ni-YSZ/YSZ/BSCF and Ni-YSZ/YSZ/LSM-YSZ under a constant current density of $0.45 \text{ A}\cdot\text{cm}^{-2}$ in electrolysis mode at 800°C with steam to H_2 of 70:30 for 80h was observed, as shown in Fig. 4.10. The single cell having BSCF and LSM-YSZ anode exhibited relative much lower performance. Initial potential of 2.88V for BSCF anode and 3.48V for LSM-YSZ anode was required for current density of $0.45 \text{ A}\cdot\text{cm}^{-2}$. It can be clearly seen that a performance decay was observed for the cell having BSCF anode (degradation rate of $0.0123\text{V}\cdot\text{h}^{-1}$) and LSM-YSZ anode (degradation rate of $0.0204\text{V}\cdot\text{h}^{-1}$) For the single cell having BSCFTa0.10 anode, the cell showed better stability during 80h (degradation rate of $0.0027\text{V}\cdot\text{h}^{-1}$), indicating that partial substituting of BSCF with Ta^{5+} improved the stability of BSCF.

The I/V response and EIS measurement before and after durability test ($-0.45 \text{ A}\cdot\text{cm}^{-2}$, 80h, 800°C) were measured, as shown in Fig. 4.11. As can be seen in Fig. 4.11(a) and 4.11(b), the current density of single cell was significantly lower, which can be resulted to the lower H_2 production. The H_2 production rate were 0.06, 0.10 and $2.58 \mu\text{mol}\cdot\text{s}^{-1}$ for single cell having LSM-YSZ, BSCF and BSCFTa0.10 anode, respectively. The decreasing of current density corresponding to increasing cell resistance, as shown in Fig. 4.11(c). For EIS measurement, the ohmic resistance and total polarization resistance were increased of all single cell. For Ni-YSZ/YSZ/BSCF, the ohmic resistance increased from 10.48 to $16.26\Omega\cdot\text{cm}^2$ and the total polarization resistance increased from 3.32 to $6.67\Omega\cdot\text{cm}^2$. For Ni-YSZ/YSZ/BSCFTa0.10, the ohmic resistance increased from 0.44 to $1.68\Omega\cdot\text{cm}^2$ and the total polarization resistance increased from 0.23 to $1.06\Omega\cdot\text{cm}^2$. And for Ni-YSZ/YSZ/LSM-YSZ, the ohmic resistance increased from 3.31 to $10.07\Omega\cdot\text{cm}^2$ but the total polarization resistance slightly decreased from 9.29 to $6.91\Omega\cdot\text{cm}^2$. It can be indicated that single cell having BSCF anode showed the highest increase of total polarization resistance, whereas single cell having BSCFTa0.10 anode showed a lowest increase with operating time.

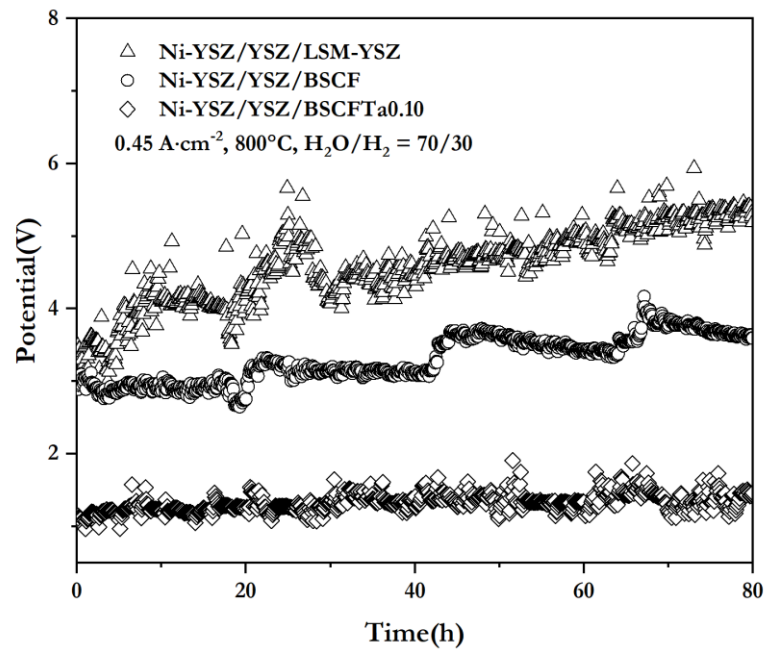
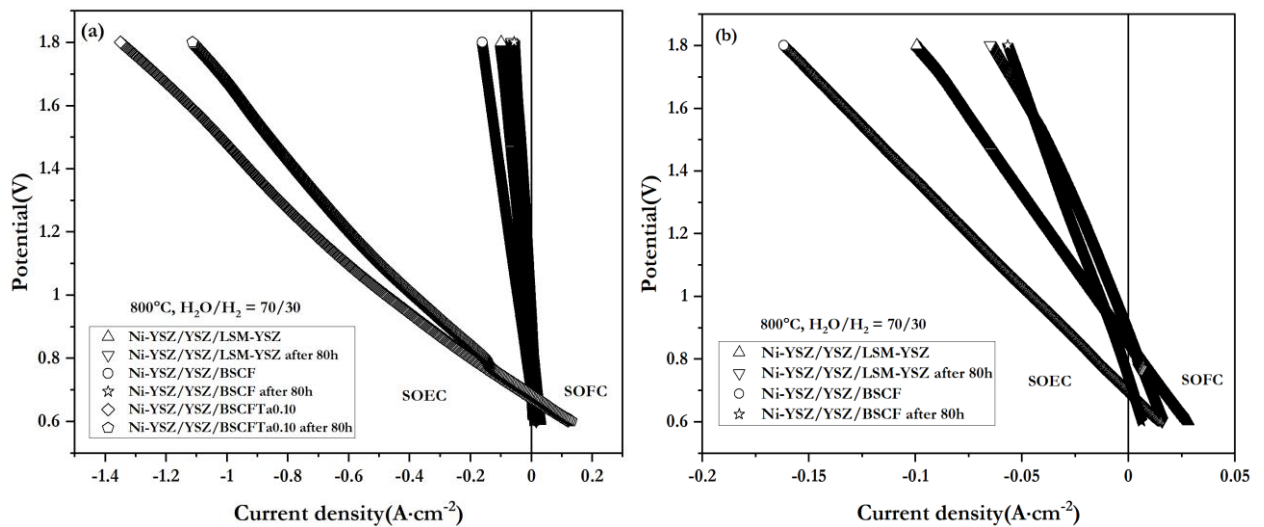


Figure 4.10 Single cell potential monitoring under electrolysis mode for 80h. ($0.45\text{A}\cdot\text{cm}^{-2}$, 800°C and steam to H_2 ratio of 70:30) of Ni-YSZ/YSZ/LSM-YSZ, Ni-YSZ/YSZ/BSCF and Ni-YSZ/YSZ/BSCFTa0.10



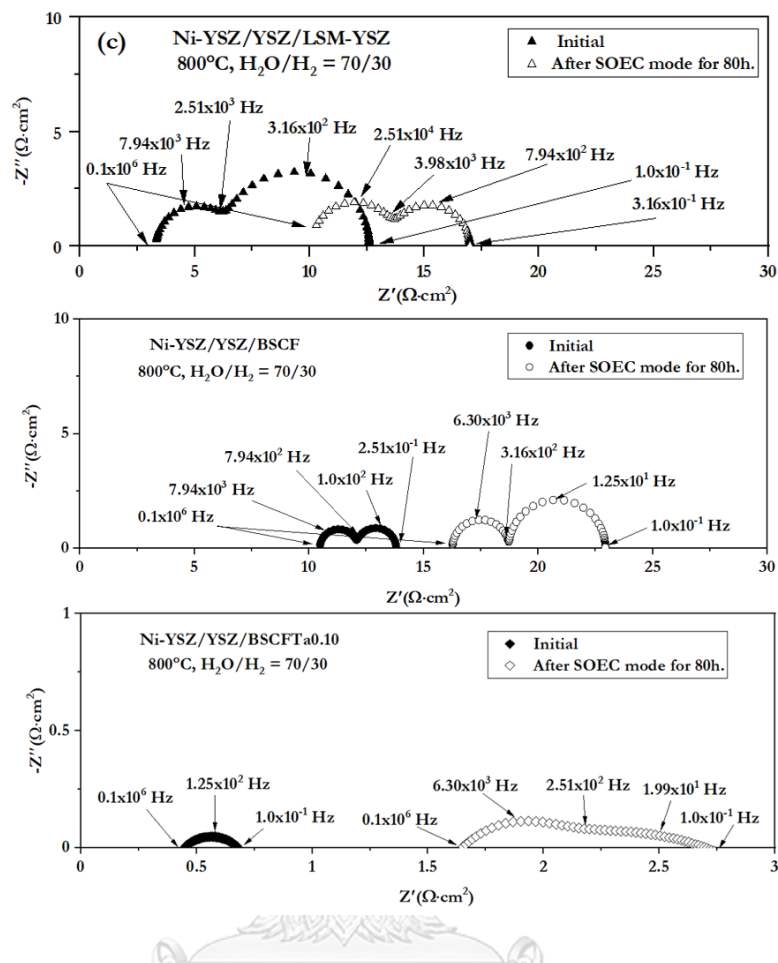


Figure 4.11 Comparing electrochemical performance before and after operated under electrolysis mode for 80h. ($0.45\text{A}\cdot\text{cm}^{-2}$, 800°C and steam to H_2 ratio of 70:30): **(a)** The I/V response of Ni-YSZ/YSZ/BSCF, Ni-YSZ/YSZ/BSCFTa0.10 and Ni-YSZ/YSZ/LSM-YSZ; **(b)** The magnified scale I/V response of Ni-YSZ/YSZ/BSCF and Ni-YSZ/YSZ/LSM-YSZ; and **(c)** The EIS response

As can be seen in Fig. 4.12, the cross-sectional SEM images of single cell having BSCF and BSCFTa0.10 anode after prolong operation under electrolysis mode for 80h were observed. It is seen that both of BSCF and BSCFTa0.10 electrode have sign of detachment, as shown in Fig. 4.12(a) and (b), while Fig. 4.12(d) and (e) shows the BSCF and BSCFTa0.10 were barely remained on electrolyte layer. Conversely, LSM-YSZ exhibited no sign of peeling off from the electrolyte layer, as shown in Fig. 4.12(c) and (f), respectively. The thickness of anode was 4.70, 9.78 and 19.86 μm for

BSCF, BSCFTa0.10 and LSM-YSZ, respectively. It was reported that TEC of LSM-YSZ ($11.5 \times 10^{-6} \text{ K}^{-1}$) was nearly to YSZ electrolyte ($10.8 \times 10^{-6} \text{ K}^{-1}$), which was a compatible TEC and resulting in a compatibility between LSM-YSZ anode and YSZ electrolyte [56]. In case of Co-based perovskite anode, the delamination of oxygen electrode can be observed due to a large TEC of Co during thermal expansion effected to the thermal mismatching of BSCF was larger than YSZ electrolyte [57, 58]. Normally, TEC of BSCF was $19.6 \times 10^{-6} \text{ K}^{-1}$ in the high temperature region (800-1000°C), while in the intermediate temperature region (600-700°C) was between $15.62\text{-}16.76 \times 10^{-6} \text{ K}^{-1}$ [59-62]. For BSCFTa0.10, the value of TEC was calculated. It was a smaller TEC of BSCFTa0.10 ($15.71 \times 10^{-6} \text{ K}^{-1}$) when compared with BSCF because partial substituting of Ta^{5+} on BSCF will diminish the Co content and stabilized the charge cation at B-site on perovskite structure. However, it was more difference of TEC between BSCFTa0.10 and YSZ electrolyte, which can be affected to the delamination on oxygen electrode that shows on SEM images given below.

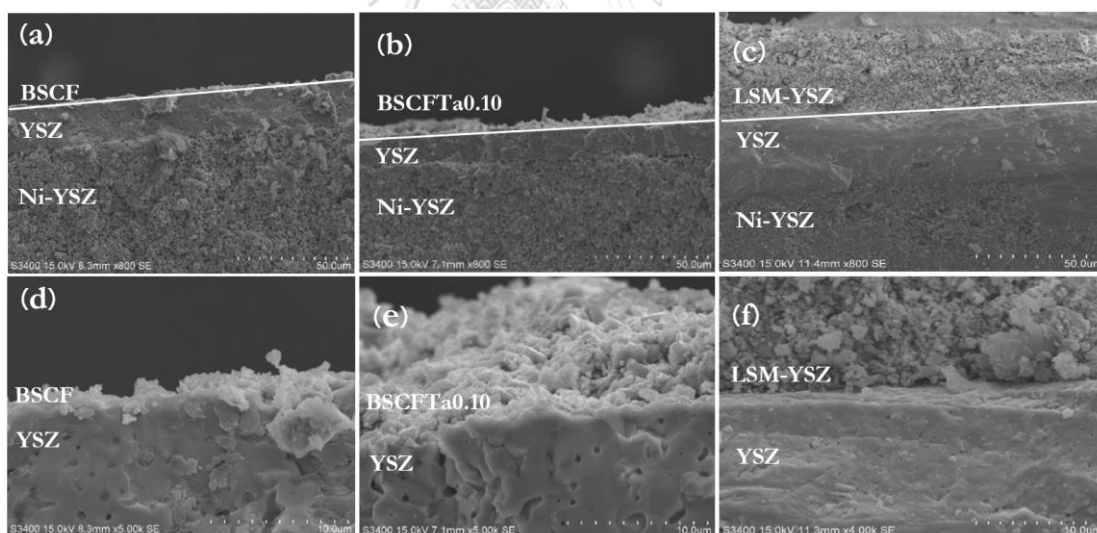


Figure 4.12 SEM images of BSCF and BSCFTa0.10 anode after durability test under electrolysis mode for 80h. ($0.45 \text{ A} \cdot \text{cm}^{-2}$, 800°C and steam to H_2 ratio of 70:30): **(a), (b) and (c)** illustrate the cross-section of Ni-YSZ/YSZ/BSCF, Ni-YSZ/YSZ/BSCFTa0.10 and Ni-YSZ/YSZ/LSM-YSZ cell, respectively; **(d), (e) and (f)** illustrate the magnified scale of cross-section of cell between BSCF and YSZ layer, BSCFTa0.10 and YSZ layer and LSM-YSZ and YSZ layer, respectively.

CHAPTER V

CONCLUSIONS

5.1 Conclusions

$\text{Ba}_{0.5}\text{Sr}_{0.5}(\text{Co}_{0.8}\text{Fe}_{0.2})_{1-x}\text{Ta}_x\text{O}_{3.8}$ ($0 \leq x \leq 0.2$) powder were successfully synthesized by citrate-EDTA complexing method. BSCF and BSCFTa0.05 exhibited single phase perovskite, which were obtained by calcination the precursor at 950°C for 4h. While segregation of Ta_2O_5 and Ta_3N_5 were observed in other samples. For TGA analysis, no difference on thermal stability on BSCF and BSCFTa. Moreover, the influence of ambient air is acceptable in BSCFTa structure due to operating BSCFTa as the anode on SOEC under low oxygen partial pressure (N_2) will introduce the oxygen vacancies, which can be effected to the larger weight loss and structural instability. According to the XPS spectra, the valence state of O1s and Co2p were characterized. Increasing the Ta^{5+} -doping content would decrease the ratio of $\text{O}_{\text{adsorbed}}/\text{O}_{\text{lattice}}$, which indicated to the lower of oxygen vacancy and corresponded to the greater stability performance on oxygen electrode. Conversely, increasing the partial substituting of Ta^{5+} on BSCF would increase the ratio of $\text{Co}^{3+}/\text{Co}^{4+}$, which mean the valence state on Co ions change from Co^{3+} to Co^{4+} , which also diminish the oxygen vacancy in the lattice structure. In addition, percentage of Co^{3+} and Co^{4+} can be calculated to the tolerance factor. The results exhibited the tolerance factor value is nearly to 1, which mean the Ta^{5+} led to maintain the structural stability of BSCF.

The area specific resistance of oxygen electrode were studied on symmetrical half-cells. In this study, BSCFTa0.10 shows the lowest total polarization resistance of 1.48eV that consistent with the lowest area specific resistance. Hence, BSCFTa0.10 shown the optimum Ta^{5+} content, which can be improved the balance between oxygen permeability on electrochemical performance and the stability for long term operation.

The electrochemical performance of single cell having BSCF and LSM-YSZ basic anode comparing to BSCFTa0.10 anode were studied. BSCFTa0.10 exhibited the

greatest performance anode in term of cell performance and chemical stability. The current density of Ni-YSZ/YSZ/BSCFTa0.10 was 8.3 times higher than Ni-YSZ/YSZ/BSCF at 1.8V, which indicated the higher of H₂ production rate. The cell performance of cathode-supported having BSCFTa0.10 anode increased with increasing the operating temperature, while the steam content was significantly affected to the cell performance. The current density increased when increasing the steam to H₂ ratio. And the performance decay of single cell under electrolysis mode for 80h (0.45 A·cm⁻², 800°C and steam to H₂ ratio of 70:30) was observed. The cell with BSCFTa0.10 as anode has the best chemical stability anode as the result of partial substituting with highly valence state of Ta⁵⁺ leading to a better performance. The result of cell performance after prolong operation were supported by I/V curve and EIS measurement. The current density of all single cell were decreased. Furthermore, the shift in ohmic resistance can be related to the change on oxygen electrode layer as shown on SEM images.

5.2 Recommendations

Composition of each anode and crystallite size of Ba_{0.5}Sr_{0.5}(Co_{0.8}Fe_{0.2})_{1-x}Ta_xO_{3.δ} (0 ≤ x ≤ 0.2) powder are required a further investigation by Inductively coupled plasma (ICP) and TEM (Transmission electron microscopy), respectively. TEC of each anode should be calculated by weight ratio of composition and to obtain a precise TEC value, further work is needed using dilatometer.

REFERENCES

- [1] Energy USDo. Energy policy act of 1992. In: Office EDVT, editor.1992.
- [2] Andika R, Nandiyanto ABD, Putra ZA, Bilad MR, Kim Y, Yun CM, et al. Co-electrolysis for power-to-methanol applications. *Renewable and Sustainable Energy Reviews*. 2018;95:227-41.
- [3] Bo Jiang HC, Longfei Luo, Xionggang Lu, Naijun Zhang, Jizhong Liu Oxygen permeation and phase structure properties of partially A-site substituted $\text{BaCo}_{0.7}\text{Fe}_{0.225}\text{Ta}_{0.075}\text{O}_{3-\delta}$ perovskites *Energy chemistry*. 2014;23:164-70.
- [4] Shao Z, Yang W, Cong Y, Dong H, Tong J, Xiong G. Investigation of the permeation behavior and stability of a $\text{Ba}_{0.5}\text{Sr}_{0.5}\text{Co}_{0.8}\text{Fe}_{0.2}\text{O}_{3-\delta}$ oxygen membrane. *J Membr Sci*. 2000;172:177-88.
- [5] Shao ZP, Yang WS, Cong Y, Dong H, Tong JH, Xiong GX. Investigation of the permeation behavior and stability of a $\text{Ba}_{0.5}\text{Sr}_{0.5}\text{Co}_{0.8}\text{Fe}_{0.2}\text{O}_{3-\delta}$ oxygen membrane. *J Membr Sci*. 2000;172:177-88.
- [6] Egorova YV, Scherb T, Schumacher G, Bouwmeester HJM, Filatova EO. Soft X-ray absorption spectroscopy study of $(\text{Ba}_{0.5}\text{Sr}_{0.5})(\text{Co}_{0.8}\text{Fe}_{0.2})_{1-x}\text{Nb}_x\text{O}_{3-\delta}$ with different content of Nb (5%–20%). *J Alloys Compd*. 2015;650:848-52.
- [7] Baumann S, Schulze-Küppers F, Roitsch S, Betz M, Zwick M, Pfaff EM, et al. Influence of sintering conditions on microstructure and oxygen permeation of $\text{Ba}_{0.5}\text{Sr}_{0.5}\text{Co}_{0.8}\text{Fe}_{0.2}\text{O}_{3-\delta}$ (BSCF) oxygen transport membranes. *J Membr Sci*. 2010;359:102-9.
- [8] Prabhakaran K, Beigh MO, Lakra J, Gokhale NM, Sharma SC. Characteristics of 8mol% yttria stabilized zirconia powder prepared by spray drying process. *J Mater Process Technol*. 2007;189:178-81.
- [9] Ni M, Leung MKH, Leung DYC. Technological development of hydrogen production by solid oxide electrolyzer cell (SOEC). *Int J Hydrogen Energy*. 2008;33:2337-54.
- [10] Dwivedi S. Solid oxide fuel cell: Materials for anode, cathode and electrolyte. *Int J Hydrogen Energy*. 2020;45:23988-4013.
- [11] Gangopadhyay S, Inerbaev T, Masunov AE, Altilio D, Orlovskaya N. Structural characterization combined with the first principles simulations of barium/strontium

- cobaltite/ferrite as promising material for solid oxide fuel cells cathodes and high-temperature oxygen permeation membranes. *ACS Appl Mater Interfaces*. 2009;1:1512-9.
- [12] Minh NQ, Takahashi T. *Science and Technology of Ceramic Fuel Cells*: Elsevier Science; 1995.
- [13] Keane M, Mahapatra MK, Verma A, Singh P. LSM–YSZ interactions and anode delamination in solid oxide electrolysis cells. *Int J Hydrogen Energy*. 2012;37:16776-85.
- [14] Tai LW, Nasrallah MM, Anderson HU, Sparlin DM, Sehlin SR. Structure and electrical properties of $\text{La}_{1-x}\text{Sr}_x\text{Co}_{1-y}\text{Fe}_y\text{O}_3$. Part 2. The system $\text{La}_{1-x}\text{Sr}_x\text{Co}_{0.2}\text{Fe}_{0.8}\text{O}_3$. *Solid State Ionics*. 1995;76:273-83.
- [15] Shao Z, Haile S. A High Performance Cathode for the Next Generation Solid-Oxide Fuel Cells. *Nature*. 2004;431:170-3.
- [16] Svarcova S. Structural instability of cubic perovskite $\text{Ba}_x\text{Sr}_{1-x}\text{Co}_{1-y}\text{Fe}_y\text{O}_{3-\delta}$. *Solid State Ionics*. 2008;178:1787-91.
- [17] Reshmi Varma PC. Low-Dimensional Perovskites. *Perovskite Photovoltaics 2018*. p. 197-229.
- [18] Zhang JL, Hong GY. Nonstoichiometric Compounds. *Modern Inorganic Synthetic Chemistry 2017*. p. 329-54.
- [19] Peña MA, Fierro JL. Chemical structures and performance of perovskite oxides. *Chem Rev*. 2001;101:1981-2017.
- [20] Li Z, Wei B, Lü Z, Huang X, Su W. Structure, electrical and thermal properties of $(\text{Ba}_{0.5}\text{Sr}_{0.5})_{1-x}\text{Gd}_x\text{Co}_{0.8}\text{Fe}_{0.2}\text{O}_{3-\delta}$ perovskite as a solid-oxide fuel cell cathode. *Solid State Ionics*. 2012;207:38-43.
- [21] Zhang J, Zhang Z, Chen Y, Xu X, Zhou C, Yang G, et al. Materials design for ceramic oxygen permeation membranes: Single perovskite vs. single/double perovskite composite, a case study of tungsten-doped barium strontium cobalt ferrite. *J Membr Sci*. 2018;566:278-87.
- [22] Shubnikova EV BO, Nemudry AP. Mixed conducting molybdenum doped BSCF materials. *Industrial and Engineering Chemistry*. 2018;59:242-50.
- [23] Bi L, Fabbri E, Traversa E. Novel $\text{Ba}_{0.5}\text{Sr}_{0.5}(\text{Co}_{0.8}\text{Fe}_{0.2})_{1-x}\text{Ti}_x\text{O}_{3-\delta}$ ($x=0, 0.05, \text{ and } 0.1$) cathode materials for proton-conducting solid oxide fuel cells. *Solid State Ionics*. 2012;214:1-5.

- [24] Cheng Y, Zhao H, Teng D, Li F, Lu X, Ding W. Investigation of Ba fully occupied A-site $\text{BaCo}_{0.7}\text{Fe}_{0.3-x}\text{Nb}_x\text{O}_{3-\delta}$ perovskite stabilized by low concentration of Nb for oxygen permeation membrane. *J Membr Sci.* 2008;322:484-90.
- [25] Li Y, Zhao H, Xu N, Shen Y, Lu X, Ding W, et al. Systematic investigation on structure stability and oxygen permeability of Sr-doped $\text{BaCo}_{0.7}\text{Fe}_{0.2}\text{Nb}_{0.1}\text{O}_{3-\delta}$ ceramic membranes. *J Membr Sci.* 2010;362:460-70.
- [26] Athayde DD, Souza DF, Silva AMA, Vasconcelos D, Nunes EHM, Diniz da Costa JC, et al. Review of perovskite ceramic synthesis and membrane preparation methods. *Ceram Int.* 2016;42:6555-71.
- [27] Matheswaran P, Rajasekhar M, Subramania A. Assisted combustion synthesis and characterization of $\text{Pr}_{0.6}\text{Sr}_{0.4}\text{MnO}_{3\pm\delta}$ nano crystalline powder as cathode material for IT-SOFC. *Ceram Int.* 2017;43:988-91.
- [28] Sunarso J, Baumann S, Serra JM, Meulenber WA, Liu S, Lin YS, et al. Mixed ionic-electronic conducting (MIEC) ceramic-based membranes for oxygen separation. *J Membr Sci.* 2008;320:13-41.
- [29] Li J, Fu Z, Wei B, Su C, Yue X, Lü Z. Tailoring tantalum doping into a perovskite ferrite to obtain a highly active and stable anode for solid oxide fuel cells. *Journal of Materials Chemistry A.* 2020.
- [30] Belenkaya IV, Matvienko AA, Nemudry AP. Phase transitions and microstructure of ferroelastic MIEC oxide $\text{SrCo}_{0.8}\text{Fe}_{0.2}\text{O}_{2.5}$ doped with highly charged Nb/Ta(v) cations. *Journal of Materials Chemistry A.* 2015;3:23240-51.
- [31] Patra H, Rout SK, Pratihari SK, Bhattacharya S. Thermal, electrical and electrochemical characteristics of $\text{Ba}_{1-x}\text{Sr}_x\text{Co}_{0.8}\text{Fe}_{0.2}\text{O}_{3-\delta}$ cathode material for intermediate temperature solid oxide fuel cells. *Int J Hydrogen Energy.* 2011;36:11904-13.
- [32] Yao C, Zhang H, Liu X, Meng J, Meng J, Meng F. A niobium and tungsten co-doped SrFeO_3 -perovskite as cathode for intermediate temperature solid oxide fuel cells. *Ceram Int.* 2019;45:7351-8.
- [33] Toprak MS, Darab M, Syvertsen GE, Muhammed M. Synthesis of nanostructured BSCF by oxalate co-precipitation – As potential cathode material for solid oxide fuel cells. *Int J Hydrogen Energy.* 2010;35:9448-54.

- [34] Zeng P, Chen Z, Zhou W, Gu H, Shao Z, Liu S. Re-evaluation of $\text{Ba}_{0.5}\text{Sr}_{0.5}\text{Co}_{0.8}\text{Fe}_{0.2}\text{O}_{3-\delta}$ perovskite as oxygen semi-permeable membrane. *J Membr Sci.* 2007;291:148-56.
- [35] Huang Y, Ding J, Xia Y, Miao L, Li K, Zhang Q, et al. $\text{Ba}_{0.5}\text{Sr}_{0.5}\text{Co}_{0.8-x}\text{Fe}_{0.2}\text{Nb}_x\text{O}_{3-\delta}$ ($x \leq 0.1$) as cathode materials for intermediate temperature solid oxide fuel cells with an electron-blocking interlayer. *Ceram Int.* 2020;46:10215-23.
- [36] Norman C, Leach C. In situ high temperature X-ray photoelectron spectroscopy study of barium strontium iron cobalt oxide. *J Membr Sci.* 2011;382:158-65.
- [37] Jung J-I, Edwards DD. X-ray photoelectron (XPS) and Diffuse Reflectance Infra Fourier Transformation (DRIFT) study of $\text{Ba}_{0.5}\text{Sr}_{0.5}\text{Co}_x\text{Fe}_{1-x}\text{O}_{3-\delta}$ (BSCF: $x=0-0.8$) ceramics. *J Solid State Chem.* 2011;184:2238-43.
- [38] Liu B, Zhang Y, Tang L. X-ray photoelectron spectroscopic studies of $\text{Ba}_{0.5}\text{Sr}_{0.5}\text{Co}_{0.8}\text{Fe}_{0.2}\text{O}_{3-\delta}$ cathode for solid oxide fuel cells. *Int J Hydrogen Energy.* 2009;34:435-9.
- [39] Yao C, Meng J, Liu X, Zhang X, Meng F, Wu X, et al. Effects of Bi doping on the microstructure, electrical and electrochemical properties of $\text{La}_{2-x}\text{Bi}_x\text{Cu}_{0.5}\text{Mn}_{1.5}\text{O}_6$ ($x = 0, 0.1$ and 0.2) perovskites as novel cathodes for solid oxide fuel cells. *Electrochimica Acta.* 2017;229:429-37.
- [40] Yang X, Li R, Yang Y, Wen G, Tian D, Lu X, et al. Improving stability and electrochemical performance of $\text{Ba}_{0.5}\text{Sr}_{0.5}\text{Co}_{0.2}\text{Fe}_{0.8}\text{O}_{3-\delta}$ electrode for symmetrical solid oxide fuel cells by Mo doping. *J Alloys Compd.* 2020;831.
- [41] Hung IM, Laing C-Y. Synthesis and Characterization of $\text{Ba}_{0.5}\text{Sr}_{0.5}\text{Co}_{0.8}\text{Fe}_{0.2}\text{O}_{3-\delta}$ for Intermediate Temperature Solid Oxide Fuel Cell Cathode by Solid-State Reaction, Pechini and Citrate-EDTA Complexing Methods. *ECS Transactions.* 2009;25.
- [42] Wang F, Nakamura T, Yashiro K, Mizusaki J, Amezawa K. Effect of Nb doping on the chemical stability of BSCF-based solid solutions. *Solid State Ionics.* 2014;262:719-23.
- [43] Yi J, Schroeder M, Weirich T, Mayer J. Behavior of $\text{Ba}(\text{Co}, \text{Fe}, \text{Nb})\text{O}_{3-\delta}$ Perovskite in CO_2 -Containing Atmospheres: Degradation Mechanism and Materials Design. *Chem Mater.* 2010;22:6246-53.
- [44] Ghaffari M, Shannon M, Hui H, Tan OK, Irannejad A. Preparation, surface state and band structure studies of $\text{SrTi}_{(1-x)}\text{Fe}_{(x)}\text{O}_{(3-\delta)}$ ($x=0-1$) perovskite-type nano structure by X-

ray and ultraviolet photoelectron spectroscopy. *Surf Sci.* 2012;606:670-7.

[45] Wang L, Dou R, Bai M, Li Y, Hall D, Chen Y. Characterisation of microstructure and hardness of perovskite-structured $\text{Ba}_{0.5}\text{Sr}_{0.5}\text{Co}_{0.8}\text{Fe}_{0.2}\text{O}_{3-\delta}$ under different sintering conditions. *J Eur Ceram Soc.* 2016;36:1659-67.

[46] Li M, Zhou W, Peterson VK, Zhao M, Zhu Z. A comparative study of $\text{SrCo}_{0.8}\text{Nb}_{0.2}\text{O}_{3-\delta}$ and $\text{SrCo}_{0.8}\text{Ta}_{0.2}\text{O}_{3-\delta}$ as low-temperature solid oxide fuel cell cathodes: effect of non-geometry factors on the oxygen reduction reaction. *Journal of Materials Chemistry A.* 2015;3:24064-70.

[47] Kim Y-M, Kim-Lohsoontorn P, Baek S-W, Bae J. Electrochemical performance of unsintered $\text{Ba}_{0.5}\text{Sr}_{0.5}\text{Co}_{0.8}\text{Fe}_{0.2}\text{O}_{3-\delta}$, $\text{La}_{0.6}\text{Sr}_{0.4}\text{Co}_{0.8}\text{Fe}_{0.2}\text{O}_{3-\delta}$, and $\text{La}_{0.8}\text{Sr}_{0.2}\text{MnO}_{3-\delta}$ cathodes for metal-supported solid oxide fuel cells. *Int J Hydrogen Energy.* 2011;36:3138-46.

[48] Kamlungsua K, Su P-C. Moisture-dependent electrochemical characterization of $\text{Ba}_{0.2}\text{Sr}_{1.8}\text{Fe}_{1.5}\text{Mo}_{0.5}\text{O}_{6-\delta}$ as the fuel electrode for solid oxide electrolysis cells (SOECs). *Electrochimica Acta.* 2020;355.

[49] Irvine JTS, Sinclair DC, West AR. Electroceramics: Characterization by Impedance Spectroscopy. *Adv Mater.* 1990;2:132-8.

[50] Dey S, Mukhopadhyay J, Lenka RK, Patro PK, Sharma AD, Mahata T, et al. Synthesis and characterization of Nanocrystalline $\text{Ba}_{0.6}\text{Sr}_{0.4}\text{Co}_{0.8}\text{Fe}_{0.2}\text{O}_3$ for application as an efficient anode in solid oxide electrolyser cell. *Int J Hydrogen Energy.* 2020;45:3995-4007.

[51] Bevilacqua M, Montini T, Tavagnacco C, Fonda E, Fornasiero P, Graziani M. Preparation, Characterization, and Electrochemical Properties of Pure and Composite $\text{LaNi}_{0.6}\text{Fe}_{0.4}\text{O}_3$ -Based Cathodes for IT-SOFC. *Chem Mater.* 2007;19:5926-36.

[52] Kong J, Zhang Y, Deng C, Xu J. Synthesis and electrochemical properties of LSM and LSF perovskites as anode materials for high temperature steam electrolysis. *J Power Sources.* 2009;186:485-9.

[53] Khan MS, Xu X, Li M, Rehman A-u, Knibbe R, Yago AJ, et al. Evaluation of $\text{SrCo}_{0.8}\text{Nb}_{0.2}\text{O}_{3-\delta}$, $\text{SrCo}_{0.8}\text{Ta}_{0.2}\text{O}_{3-\delta}$ and $\text{SrCo}_{0.8}\text{Nb}_{0.1}\text{Ta}_{0.1}\text{O}_{3-\delta}$ as air electrode materials for solid oxide electrolysis and reversible solid oxide cells. *Electrochimica Acta.* 2019;321.

[54] Shen F, Lu K. Comparison of Different Perovskite Cathodes in Solid Oxide Fuel Cells. *Fuel Cells.* 2018;18:457-65.

- [55] Zheng H, Tian Y, Zhang L, Chi B, Pu J, Jian L. $\text{La}_{0.8}\text{Sr}_{0.2}\text{Co}_{0.8}\text{Ni}_{0.2}\text{O}_{3-\delta}$ impregnated oxygen electrode for $\text{H}_2\text{O}/\text{CO}_2$ co-electrolysis in solid oxide electrolysis cells. *J Power Sources*. 2018;383:93-101.
- [56] Li N, Mahapatra MK, Singh P. Sintering of porous strontium doped lanthanum manganite-yttria stabilized zirconia composite in controlled oxygen atmosphere at 1400 °C. *J Power Sources*. 2013;221:57-63.
- [57] Kim-Lohsoontorn P, Brett DJL, Laosiripojana N, Kim YM, Bae JM. Performance of solid oxide electrolysis cells based on composite $\text{La}_{0.8}\text{Sr}_{0.2}\text{MnO}_{3-\delta}$ – yttria stabilized zirconia and $\text{Ba}_{0.5}\text{Sr}_{0.5}\text{Co}_{0.8}\text{Fe}_{0.2}\text{O}_{3-\delta}$ oxygen electrodes. *Int J Hydrogen Energy*. 2010;35:3958-66.
- [58] Temluxame P, Puengjinda P, Peng-ont S, Ngampuengpis W, Sirimungkalakul N, Jiwanuruk T, et al. Comparison of ceria and zirconia based electrolytes for solid oxide electrolysis cells. *Int J Hydrogen Energy*. 2020.
- [59] Wei B, Lü Z, Li S, Liu Y, Liu K, Su W. Thermal and Electrical Properties of New Cathode Material $\text{Ba}_{0.5}\text{Sr}_{0.5}\text{Co}_{0.8}\text{Fe}_{0.2}\text{O}_{3-\delta}$ for Solid Oxide Fuel Cells. *Electrochem Solid-State Lett*. 2005;8.
- [60] Wei B, Lü Z, Huang X, Miao J, Sha X, Xin X, et al. Crystal structure, thermal expansion and electrical conductivity of perovskite oxides $\text{Ba}_x\text{Sr}_{1-x}\text{Co}_{0.8}\text{Fe}_{0.2}\text{O}_{3-\delta}$ ($0.3 \leq x \leq 0.7$). *J Eur Ceram Soc*. 2006;26:2827-32.
- [61] Qingshanzhu, Tonganjin, Yongwang. Thermal expansion behavior and chemical compatibility of $\text{Ba}_x\text{Sr}_{1-x}\text{Co}_{1-y}\text{Fe}_y\text{O}_{3-\delta}$ with 8YSZ and 20GDC. *Solid State Ionics*. 2006;177:1199-204.
- [62] Li D. Low Thermal Expansion of $\text{Ba}_{0.5}\text{Sr}_{0.5}\text{Co}_{0.7}\text{Fe}_{0.2}\text{Mn}_{0.1}\text{O}_{3-\delta}$ cathode Material. *International Journal of Electrochemical Science*. 2018:5219-27.



APPENDIX

จุฬาลงกรณ์มหาวิทยาลัย
CHULALONGKORN UNIVERSITY

APPENDIX

APPENDIX A: Crystallite size

The crystallite size of synthesized powder was calculated using the Scherrer equation as shown in Fig. A.1 and Eq. (A.1), respectively.

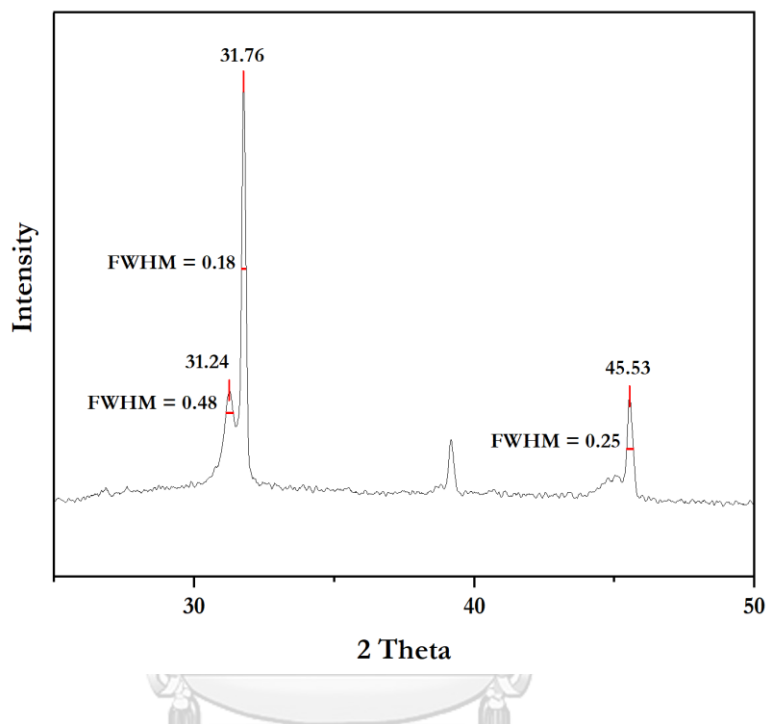


Figure A.1 Magnified scale at 2 Theta angles between 30° and 50°, which were the position of 3 highest peak on XRD graph of BSCFTa0.10 anode

$$D = \frac{K\lambda}{\beta_{FWHM}\cos\theta} \quad (A.1)$$

Where K is Scherrer constant (a typical value of 0.94); λ is the wavelength of x-ray (in this case: 0.1541nm for Cu K-alpha); β_{FWHM} is the full width at half-maximum of the diffraction peak, θ is the Bragg angle and D is crystallite size(nm).

θ calculation:

$$2\theta_1 = 31.24 \text{ and } \theta_1 = 15.62$$

$$2\theta_2 = 31.76 \text{ and } \theta_2 = 15.88$$

$$2\theta_3 = 45.53 \text{ and } \theta_3 = 22.76$$

β calculation:

β value can be calculated from FWHM that interpolate from XRD results, as shown in Fig. A.1

$$\beta_1 = (0.48 \times 2\pi) / 360 = 0.00837$$

$$\beta_2 = (0.18 \times 2\pi) / 360 = 0.00314$$

$$\beta_3 = (0.25 \times 2\pi) / 360 = 0.00436$$

Crystallite size of BSCFTa0.10:

$$D_1 = (0.94 \times 0.1541) / (0.00837 \cos(15.62)) = 17.96 \text{ nm}$$

$$D_2 = (0.94 \times 0.1541) / (0.00314 \cos(15.88)) = 47.96 \text{ nm}$$

$$D_3 = (0.94 \times 0.1541) / (0.00436 \cos(22.76)) = 36.02 \text{ nm}$$

Hence, the average crystallite size of BSCFTa0.10:

$$= (17.96 + 47.96 + 36.02) / 3$$

$$= 33.98 \text{ nm}$$

APPENDIX B: Lattice parameter

The lattice parameter was calculated using the Bragg's law equation as shown in Eq. (B.1) and Eq. (B.2), respectively.

$$n\lambda = 2d\sin\theta \quad (\text{B.1})$$

where n is an integer; λ is the wavelength of the x-ray (1.54 Å); d is the spacing of the crystal layers; and θ is the angle between incident ray and the scatter plane

Lattice parameter equation for cubic structure:

$$\left(\frac{1}{d^2}\right) = (h^2 + k^2 + l^2)\left(\frac{1}{a^2}\right) \quad (\text{B.2})$$

when d is the spacing of the crystal layers; a is lattice parameter; and h, k, l are spacing between lattice planes

θ and plane (h, k, l) were found from XRD pattern and data of JCPDS No. 01-079-5253 (BSCF data), respectively. For BSCFTa0.10, θ and plane (h, k, l) were used to calculating the lattice parameter as below.

d calculation:

$$n\lambda = 2d\sin\theta$$

$$\left(\frac{1}{d^2}\right) = 4\sin^2\theta/\lambda^2$$

$$\text{At } 2\theta = 31.76 \text{ and } \theta = 15.88, \quad \left(\frac{1}{d^2}\right) = 4\sin^2(15.88)/1.54^2 = 0.1261$$

Then substituted $\left(\frac{1}{d^2}\right)$ and (h, k, l) into Eq. (C.2)

$$\text{At } (1, 1, 0) \quad 0.1262 = (1^2 + 1^2 + 0^2)\left(\frac{1}{a^2}\right)$$

Hence, lattice parameter: $a = 3.9825 \text{ \AA}$

APPENDIX C: Tolerance factor

The Goldschmidt tolerance factor (t) was calculated using Eq. (C.1), Eq. (C.2) and Eq. (C.3):

$$t = \frac{r_A + r_O}{\sqrt{2} (r_B + r_O)} \quad (C.1)$$

$$t = \frac{[(0.5 \cdot r_{Ba^{2+}}) + (0.5 \cdot r_{Sr^{2+}}) + r_O]}{\sqrt{2} [(0.8 \cdot (1-x) \cdot y) \cdot r_{Co^{3+}}] + (0.8 \cdot (1-x) \cdot (1-y) \cdot r_{Co^{4+}}) + (0.2 \cdot (1-x) \cdot r_{Fe^{3+}}) + ((x) \cdot r_{Ta^{5+}}) + r_O]} \quad (C.2)$$

$$t = \frac{[(0.5 \cdot r_{Ba^{2+}}) + (0.5 \cdot r_{Sr^{2+}}) + r_O]}{\sqrt{2} [(0.8 \cdot (1-x) \cdot y) \cdot r_{Co^{3+}}] + (0.8 \cdot (1-x) \cdot (1-y) \cdot r_{Co^{4+}}) + (0.2 \cdot (1-x) \cdot r_{Fe^{4+}}) + ((x) \cdot r_{Ta^{5+}}) + r_O]} \quad (C.3)$$

where r_{Ba} , r_{Sr} and r_O are the ionic radii of the barium, strontium cations and oxygen ion, respectively. The x is the amount of partial substituting Ta^{5+} at B-site (0, 0.05, 0.10, 0.15 and 0.20) and y is the ratio of Co^{3+} to Co^{4+} . In Eq. (C.2) and Eq. (C.3), the valence state of Fe is assumed in trivalent state and tetravalent state, respectively. The ratio of Co^{3+}/Co^{4+} in $Ba_{0.5}Sr_{0.5}(Co_{0.8}Fe_{0.2})_{1-x}Ta_xO_{3-\delta}$ ($0 \leq x \leq 0.2$) were shown in Table C.1. And ionic radius, coordination number and ionic charge of concerned metals were shown in Table C.2, respectively.

Table C.1 The ratio of Co^{3+}/Co^{4+} in $Ba_{0.5}Sr_{0.5}(Co_{0.8}Fe_{0.2})_{1-x}Ta_xO_{3-\delta}$ ($0 \leq x \leq 0.2$)

Abbreviation	x value in $Ba_{0.5}Sr_{0.5}(Co_{0.8}Fe_{0.2})_{1-x}Ta_xO_{3-\delta}$	Co^{3+}/Co^{4+}
BSCF	0	0.31
BSCFTa 0.05	0.05	0.21
BSCFTa 0.1	0.10	0.18
BSCFTa 0.15	0.15	0.23
BSCFTa 0.2	0.20	0.25

Table C.2 Ionic charge, coordination number and ionic radius of concerned metals

Metal	Ionic charge	Coordination number	Ionic radius (Å)
Ba	2 ⁺	12	1.61
Sr	2 ⁺	12	1.44
Co	2 ⁺	6	0.74
	3 ⁺	6	0.54
	4 ⁺	6	0.53
Fe	3 ⁺	6	0.55
	4 ⁺	6	0.58
Ta	5 ⁺	6	0.64
O	2 ⁻	6	1.40

As Eq. (C.2) and Eq. (C.3) the tolerance factor of perovskite anode such as BSCFTa0.10 was calculated as below.

From Eq. (C.2), Tolerance factor of BSCFTa0.10

$$t = \frac{[(0.5 \times 1.61) + (0.5 \times 1.44) + 1.40]}{\sqrt{2} [(0.8 \times (1-0.1) \times 0.18 \times 0.54) + (0.8 \times (1-0.1) \times (1-0.18) \times 0.53) + (0.2 \times (1-0.1) \times 0.55) + (0.1 \times 0.64) + 1.40]}$$

$$= 1.0625 \text{ (for Co}^{3+}, \text{Co}^{4+}, \text{Fe}^{3+}\text{)}$$

From Eq. (C.3), Tolerance factor of BSCFTa0.10

$$t = \frac{[(0.5 \times 1.61) + (0.5 \times 1.44) + 1.40]}{\sqrt{2} [(0.8 \times (1-0.1) \times 0.18 \times 0.54) + (0.8 \times (1-0.1) \times (1-0.18) \times 0.53) + (0.2 \times (1-0.1) \times 0.58) + (0.1 \times 0.64) + 1.40]}$$

$$= 1.0591 \text{ (for Co}^{3+}, \text{Co}^{4+}, \text{Fe}^{4+}\text{)}$$

APPENDIX D: Activation energy of oxygen electrode for oxygen-oxidation reaction

The activation energy of oxygen electrode such as BSCFTa0.10 was calculated from the Arrhenius plot between the ASR and a range operating temperature as shown in Fig. D.1 and Eq. (D.1), respectively

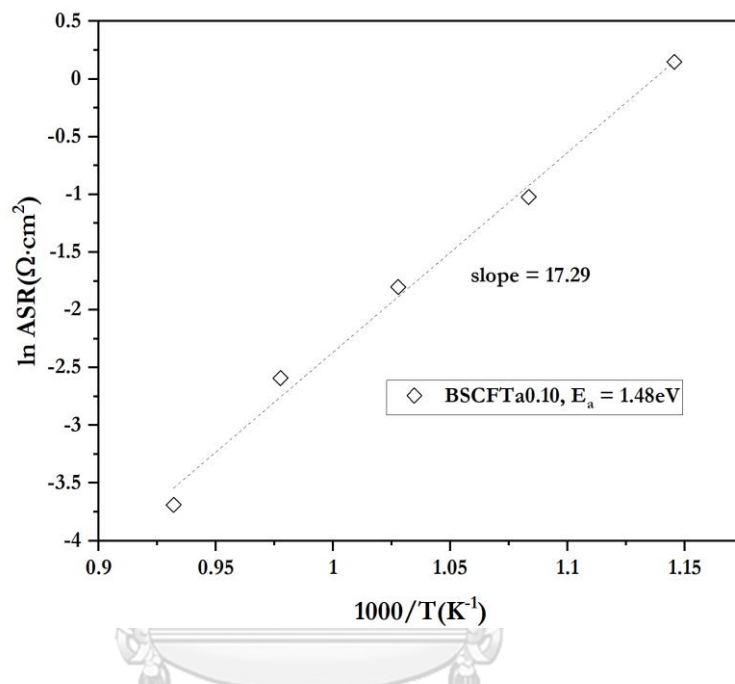


Figure D.1 Arrhenius plot of temperature dependence of the ASR of the BSCFTa0.10 anode on YSZ electrolyte

$$ASR = A \cdot e^{-E_a/K_B T} \quad (D.1)$$

where ASR is area specific resistance ($\Omega \cdot \text{cm}^2$); A is pre-exponential factor; T is the absolute temperature (K); E_a is the activation energy of oxygen electrode (eV) and K_B is the Boltzmann's constant ($8.61 \times 10^{-5} \text{ eV} \cdot \text{K}^{-1}$).

From Arrhenius plot, it was found the slope was 17.29. Hence, the activation energy of oxygen electrode for oxygen-oxidation reaction was calculated as below

$$\begin{aligned} E_a &= 17.29 \times (8.61 \times 10^{-5}) \times 1000 \\ &= 1.48 \text{ eV} \end{aligned}$$

APPENDIX E: Hydrogen production rate

The Hydrogen production rate can be calculated from I/V curve using Faraday's law as shown in Eq. (E.1)

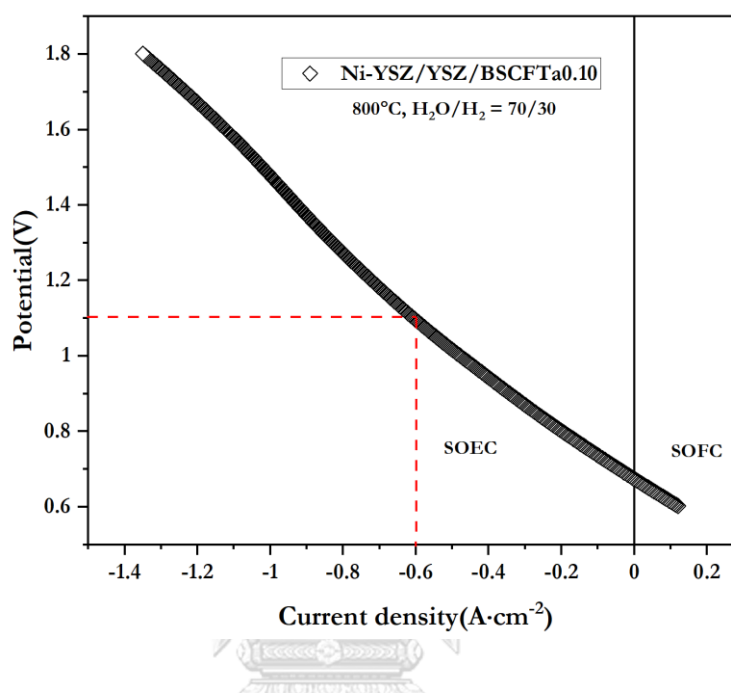


Figure E.1 The I/V response of Ni-YSZ/YSZ/BSCFTa0.10, operated at 800°C under steam to H₂ ratio of 70:30

Faraday's law of electrolysis

$$m = \frac{I}{nF} \quad (\text{E.1})$$

where m is amount of mole is generated per area; I is current (A or C·s⁻¹); n is amount of electron in reaction (in this case $n = 2$); and F is Faraday constant (96,485 C·mol⁻¹)

As be can seen in Fig. E.1, at 1.1V, current density was 0.606A·cm⁻².

Hence, hydrogen production rate = 0.606/2x96485

$$= 3.14 \mu\text{mol}\cdot\text{s}^{-1}$$

APPENDIX F: Cell degradation rate

The slope of potential (V) versus operating temperature on durability test of single cell was shown in Fig. F.1. This slope was a cell degradation rate.

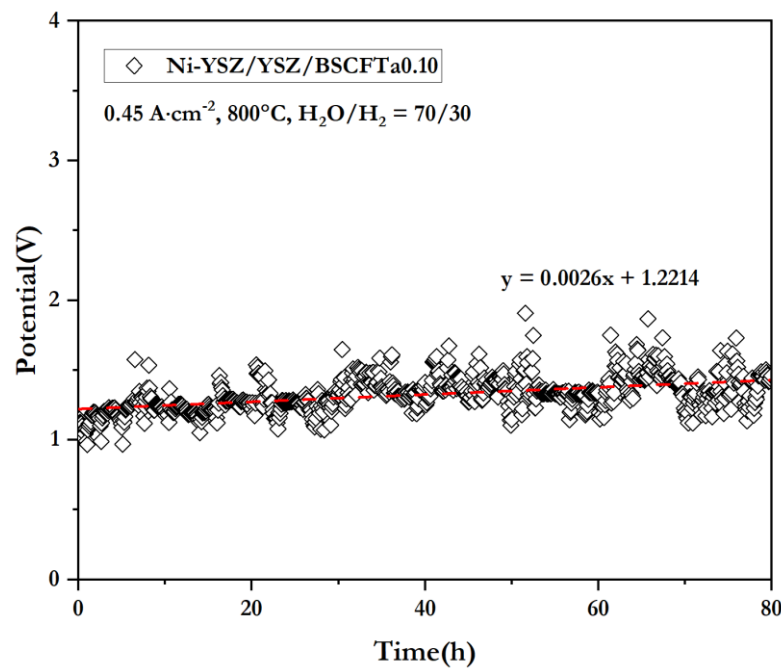


Figure F.1 Single cell potential monitoring under electrolysis mode for 80h.

($0.45 \text{ A}\cdot\text{cm}^{-2}$, 800°C and steam to H_2 ratio of 70:30) of Ni-YSZ/YSZ/BSCFTa0.10

APPENDIX G: Thermal expansion coefficient of anode layer

Thermal expansion coefficient (TEC) of anode was calculated by weight ratio of composition of anode perovskite. For BSCFTa0.10 anode, including 37wt% of Ba, 23wt% of Sr, 23wt% of Co, 5wt% of Fe and 9wt% of Ta. And TEC of pure metal was 18, 20, 14, 13 and $6.5 \cdot 10^{-6} \text{ K}^{-1}$ for Ba, Sr, Co, Fe and Ta, respectively. Hence, TEC of BSCFTa0.10 anode was calculated as below.

$$\begin{aligned} \text{TEC of BSCFTa0.10} &= [(0.37 \times 18) + (0.23 \times 20) + (0.23 \times 14) + (0.05 \times 13) + (0.09 \times 6.5)] \times 10^{-6} \\ &= 15.71 \times 10^{-6} \text{ K}^{-1} \end{aligned}$$

VITA

NAME Patthiya Prasopchokkul

DATE OF BIRTH 28 May 1996

PLACE OF BIRTH Bangkok

INSTITUTIONS ATTENDED Faculty of Engineering, Chulalongkorn University
Faculty of Engineering, Mahidol University

HOME ADDRESS 44 Prayamontart 7 Bangbon Bangkok 10150



จุฬาลงกรณ์มหาวิทยาลัย
CHULALONGKORN UNIVERSITY